Source Region and Growth Analysis of Narrowband Z-mode Emission at Saturn

J. D. Menietti[1], P. H. Yoon[2,3], D. Písa[1,4], S.-Y. Ye[1], O. Santolík[4,5], C. S. Arridge[6], D. A. Gurnett[1], and A. J. Coates[7]

[1]University of Iowa, Department of Physics and Astronomy, Iowa City, IA, USA

[2]Institute for Physical Science and Technology, University of Maryland, College Park, USA

[3]School of Space Research, Kyung Hee University, Yongin, Korea

[4]Institute of Atmospheric Physics ASCR, Prague, Czech Republic

[5]Faculty of Mathematics and Physics, Charles University, Prague, Czech Republic

[6] Dept. of Physics, Lancaster Univ., Lancaster, U.K.

[7] University College London, Mullard Space Science Laboratory, Dorking Surrey, U.K.

Corresponding author: John D. Menietti (john-menietti@uiowa.edu)

Key Points:

- Source regions of Saturn 5 kHz Z-mode emission are located.
- Wave amplitude and electron PSD are analyzed.
- Temp. anisotropy & Quasi-steady conditions near Enceladus torus drive Z-mode

Abstract

Intense Z-mode emission is observed in the lower density region near the inner edge of the Enceladus torus at Saturn, where these waves may resonate with MeV electrons. The source mechanism of this emission, which is narrow banded and most intense near 5 kHz, is not well understood. We survey the Cassini Radio and Plasma Wave Science (RPWS) data to isolate several probable source regions near the inner edge of the Enceladus density torus. Electron phase space distributions are obtained from the Cassini Electron Spectrometer (ELS), part of the Cassini Plasma Spectrometer (CAPS) investigation. We perform a plasma wave growth analysis to conclude that an electron temperature anisotropy and possibly a weak loss cone can drive the Z-mode as observed. Electrostatic electron acoustic waves and perhaps weak beam modes are also found to be unstable coincident with the Z-mode. Quasi-steady conditions near the Enceladus density torus may result in the observations of narrow band Z-mode emission at Saturn.

Introduction

Z-mode radio emission is observed at Earth in the auroral regions [Gurnett et al., 1983] and in the plasmapause associated with upper hybrid emissions [Kurth et al, 1982; Menietti and Yoon, 2006]. The emission propagates in the frequency range $f_z < f < f_{uh}$, where $f_Z = \frac{1}{2}\left(\sqrt{f_{ce}^2 + 4f_{pe}^2} - f_{ce}\right)$ (cutoff frequency) and $f_{uh} = \sqrt{f_{ce}^{\ 2} + f_{pe}^{\ 2}}$ (upper hybrid resonance) with f_{ce} and f_{pe} the cyclotron frequency and plasma frequency, respectively. Thus, the frequency range can overlap whistler mode, but with different polarization. As discussed, for example, in

Benson et al. [2006], for Z-mode frequencies $f/f_{pe} < 1$, Z-mode is left-hand polarized, while for $f/f_{pe} > 1$, it is right-hand polarized. In addition, the indices of refraction of the whistler mode and Z-mode can overlap near f_{pe} for the condition $f_{pe}/f_{ce} < 1$ as shown in Figure 4.38 of Gurnett and Bhatacharjee, 2005.

Z-mode emissions can play an important role in the acceleration of electrons in a similar manner as the whistler mode. Both wave modes can contribute to diffusive scattering of electrons [cf. Horne and Thorne, 1998; Glauert and Horne, 2005; Albert, 2007; Xiao et al, 2012]. In particular, Gu et al., 2013 have shown that Z-mode waves at Saturn may be responsible for local acceleration of electrons from hundreds of keV to tens of MeV at intermediate pitch angles. Thus, Z-mode may supplement chorus emission as a possible significant source of electron acceleration filling the radiation zones at Saturn [Shprits et al., 2012; Menietti et al., 2014; 2015].

Ye et al. [2010] have shown that narrowband 5 kHz emission at Saturn frequently propagates in the Z-mode, with the most intense observations occurring in the low density regions inside the orbit of Enceladus, where $f_{pe}/f_{ce} < 1$. Ye et al. [2010] have proposed that Saturn 5 kHz Z-mode emission may have an auroral source region. The discovery that this emission shows a rotation periodicity that is the same as Saturn Kilometric Radiation (SKR) also strongly supports an auroral source region. Menietti et al. [2011] subsequently analyzed SKR near a source region and indicated that the observed electron phase space distribution supports the wave growth of locally observed extraordinary, ordinary, and Z-mode emissions. The present study does not dispute any of these findings. However, we present here evidence that Z-mode may also have a source near the equator where the most intense emissions are observed. Menietti et al. [2015] surveyed Saturn's inner magnetosphere for Z-mode intensity as a function of frequency and position. In the current study we present results of a search of probable sources of Z-mode in this region. Electron phase space data from the Cassini Plasma Spectrometer (CAPS) electron spectrometer (ELS) [Young et all, 2004; Coates et al., 1996; Arridge et al., 2009] are used to model the expected growth rate of waves in one probable source region.

Z-mode Observations

A survey of Cassini Radio and Plasma Wave Science investigation (RPWS) [Gurnett et al., 2004] data revealed at least a half dozen examples of intense Z-mode emission in the inner Saturn magnetosphere that are candidates for source regions. All of the regions occur approximately 15 to 35 degrees away from the magnetic equator and near the inner edge of the density torus where $f_{pe}/f_{ce} < 1$. In Figure 1 we display a spectrogram of Z-mode emission for day 223 of 2008 that is characteristic of what we believe to be a probable source region. This emission is seen to be narrow-banded centered near 5 kHz at frequencies and well below the cyclotron frequency, f_{ce}. This pass was discussed in some detail in Menietti et al. [2015], but no electron phase space distribution (PSD) was available for wave growth analysis. As the spacecraft approaches the equator with increasing density and cyclotron frequency, the emission becomes quite intense for times in the range ~11:00 to ~12:15, and is close to the anticipated source region. Note also the intense broad band electrostatic emission coincident in time and overlapping in frequency with the intense Z-mode. This emission is not seen on spectrograms of the magnetic spectral density.

In order to conduct an analysis of wave growth it is necessary to obtain the electron phase space distribution in the emission source region, which may be obtained from the Electron Spectrometer (ELS), one of three sensors of the Cassini Plasma Spectrometer (CAPS). The ELS sensor is an electrostatic analyzer with a fan-shaped array of 8 anodes (detectors) that operate in an energy range from 0.6 eV to ~28 keV. Each anode has a field of view of approximately 20° with some overlap.

In Table 1 we list some of the better examples of probable source regions of Z-mode emission. Of the 6 cases studied, only day 168 of 2008 provided minimally sufficient coverage of phase space from non-obstructed ELS anodes. Obstruction occurs as a result of an anode being partially or completely blocked by the Cassini spacecraft from plasma flux or perhaps susceptible to electron flux scattered by the spacecraft into the anode. The orientation of the spacecraft is important in determining which anodes may be obstructed. The Z-mode emission observed on day 167-168, 2008 is shown in Figure 2a, centered near 5 kHz with the most intense emission observed at lower latitudes. The Cassini spacecraft during this time is in a high inclination orbit and travels from high northern to high southern latitudes crossing the magnetic equator near 04:50 on day 168. The plasma density is higher adjacent to the magnetic equator, where the most intense emission is observed. The white line is the local electron cyclotron frequency calculated from the fluxgate magnetometer measurements [Dougherty et al., 2004]. In Figure 2b we show a higher resolution plot with linear frequency scale of the most intense emission centered near a frequency of 5 kHz. The white dots are approximately 1 minute averages of the plasma frequency obtained from the Langmuir Probe instrument (part of the RPWS) on board Cassini [Wahlund et al., 2005]. No data are available beyond ~ 04:12, after which the density increases as the magnetic equator and ring plane are approached [Persoon et al., 2013]. The narrow in time, intense, broadband emission near 04:50 is the signature of the ring plane crossing at the magnetic equator. This particular magnetic equator crossing was studied in more detail by Gu et al. [2013] as mentioned in the Introduction. Electron phase space density (PSD) as a function of time during the intense 5 kHz emission is shown in Figure 3. All eight anodes of ELS are plotted, with the pitch angle (α) of each anode plotted in the bottom panel. The pattern is similar for each anode, with a decrease in electron PSD for pitch angles near 0°, and a slow increase in peak energy as a function of time. The ELS instrument during this time period collected data for all anodes every 4 seconds. However, because of the orientation of the spacecraft during this period, the time required to obtain the full range of pitch angles (0 to 180°) is approximately 3.5 minutes.

To analyze these data we have therefore singled out two periods of time, the first when the anodes are monitoring pitch angles closer to the anti-field-aligned direction, which we call Set A ($\alpha > 90°$, 03:31:59 to 03:32:01), and the second when the anodes sample pitch angles centered nearer the field-aligned direction, which we call Set B ($\alpha < 90°$, 03:35:43 to 03:35:45). We have combined both data sets, after eliminating partially obstructed anodes. The pitch angles for this analysis were obtained using the magnetic field orientation [Dougherty et al., 2004] and the Cassini ELS instrument anode directions [Young et al., 2004]. The location of the spacecraft for the time periods discussed in this investigation is near magnetic field lines connected to Saturn's radiation belts, and saturation of the ELS detectors occurs at times, but not during the times of our data set. For our analyses we have included 2 anodes nearest the anti-field aligned direction, which are partially obstructed (centered near $\alpha = 167°$ and $\alpha = 168°$). These anodes show similar fluxes to the adjacent anode ($\alpha = 154°$). Without these anodes, we have insufficient data near the anti-field-aligned direction to obtain a converging least squares fit to the data. We have also eliminated two non-obstructed anodes from Set B (centerline pitch angles of 107° and 127°) that overlap in pitch angle coverage of Set A. Sampling of electron flux for Set A is generally larger than for Set B as we noted above (Figure 3), and we avoid any additional differences due to the time delay between the sampling of Set A and Set B by eliminating any overlapping anode coverage between the two sets. No other non-obstructed anodes overlapped in coverage. A list of the anodes included in the study is given in Table 2. The resulting distribution (after mirroring the data about the $v_{\parallel}$ axis) is displayed in Figure 4a.

There are two obvious characteristics of these data. First, there is a distinct increase in electron phase space density in the anti-field-aligned direction (also seen in Figure 3), and, second, there is a temperature anisotropy (also for the anti-field-aligned direction). We have performed a non-linear least-squares fit of these data to a combination of 5 bi-Maxwellians ($w_{\parallel}$, $w_{\perp}$ are the parallel and perpendicular thermal speeds),

$$f = \sum_{s=1}^{m} f_s, \qquad f_s = \frac{n_s}{\pi^{3/2} w_{\perp s}^2 w_{\parallel s}} \exp\left(-\frac{v_{\perp}^2}{w_{\perp s}^2} - \frac{\left(v_{\parallel} - v_{ds}\right)^2}{w_{\parallel s}^2} \right). \tag{1}$$

The variable fit parameters are n, w, and $T_{\perp}/T_{\parallel}$ for each population. The fitting routine uses a gradient-expansion algorithm [cf. Bevington, p. 235-242] to compute a non-linear least squares fit to a user-supplied function with known partial derivatives. The goodness-of-fit statistic, χ^2, is weighted by the standard deviation. We initially started with three plasma populations (m=3 in equation 1), but we increased this number to 5 to obtain correspondingly better fits. For the values of m= 3, 4, and 5 populations the corresponding fits yielded χ^2 = 126, 84, and 56, respectively. In Table 3 we list the plasma parameters (except for the density) for each population (m=5) obtained from the fit, and we include in parentheses the calculated percent relative uncertainty ($|\Delta p|/p$) of each variable parameter (p). The densities in Table 3 (column 1) are the values obtained by the least-squares analysis divided by a factor of 6.2, as we now explain.

The density values in Table 3 are consistent with a plasma frequency of about 6 kHz, which is about a factor of 2.5 lower than interpreted from the data of Figure 4a, but, we have good reason to believe that the actual density in the source region is less than that interpreted from the sampled CAPS/ELS electron distribution (Figure 4a), based on Langmuir Probe (LP) measurements (Figure 2b). The discrepancy may be due in part to the sampling periods, temporal variations of the local plasma, or spacecraft charging. During the time of the data shown in Figure 4a, the average density determined by the Langmuir Probe, is 0.380 cm^{-3} corresponding to f_{pe} = 5.53 kHz (similar to Table 3). In addition, the polarization of the Z-mode emission at this time is left-handed, consistent with Z-mode propagating at a frequency less than the plasma frequency [Benson et al., 2006], but above the Z-mode cutoff, f_z.

A plot of the model distribution based on the data from Table 3 is shown in Figure 4b. We have made cuts of both the observed and model phase space distribution at pitch angles 109° and 168° as shown in Figure 5. The '+' symbol designates the observed PSD while the 'x' symbol is the model value. To produce the plots of Figures 4b and 5 the density used for each plasma population in Table 3 was multiplied by a factor of 6.2 (as discussed previously), while all the other parameters were the same. The fit to the data is good, but the model becomes increasingly too low at the largest velocities for $\alpha = 109°$. We address this problem later with the introduction of a kappa distribution fit. Positive spacecraft charging at this time prevents analysis of $E \lesssim 2$eV. There is no directly observed loss cone, but one might be conjectured assuming electron scattering over the sampling period (4 sec) may have obscured any loss cone present. At the time of the observations the spacecraft is at a latitude of ~28°. Assuming a magnetic mirror point of ~ 1.1R_s, and using the zonal harmonic magnetic field model [Connerney et al., 1982] we find that we might expect a loss cone of about 11°. This would be at the outer edge of the anode at 168° and may not be observed.

The general shape of the plasma distribution shown in Figures 4a,b (dominant plasma flux with a temperature anisotropy in the anti-field-aligned direction) is common throughout this time period of intense Z-mode emission. The primary changing parameter as a function of time is the plasma density which increases with time as the spacecraft approaches the magnetic equator and the ring plane [Persoon et al., 2013]. As we show below, the growth of Z-mode is limited by the ratio $\omega_{pe}/\Omega_{ce} < 0.35$, which thus limits the source location to times probably less than about 03:55.

Wave Growth Rate Analysis

Warm Plasma Analysis (WHAMP)

We investigate the growth of plasma waves based on the distribution model. We use the Waves in Homogeneous Anisotropic Multicomponent Plasmas (WHAMP) linear dispersion solver [Rönnmark, 1982, 1983] to search for unstable wave modes of the model distribution of Figure 4b. No nonlinear analysis is attempted. The dominant wave mode appears to be an electrostatic electron acoustic mode. The free energy source is the “Drifting 2” population, with both a temperature anisotropy and drift. Another source of the broad-banded electrostatic signatures is dust impacts near the ring plane [cf. Kurth et al., 2006; Wahlund et al., 2009; Ye et al., 2014]. We will not discuss these effects further, but they are a part of the “background” emission in this region as Cassini approaches the Enceladus ring plane. We plot the resulting dispersion and growth rate curves in Figure 6 indicating a strong growth extending up and just beyond f ~ f_{pe} = 5.97 kHz. These waves are broad-banded with a peak growth rate near 5 kHz. An analytic expression for the electron acoustic mode for a two-component plasma is given as

$$\omega_{ea}^2 = \frac{\omega_{pc}^2}{1+1/k^2\lambda_{Dh}^2}\left(1+3k^2\lambda_{Dc}^2+3\frac{n_{0h}}{n_{0c}}\frac{T_c}{T_h}\right) \quad (2)$$

where λ_D, T, and n are the Deybe length, temperature, and density for the hot (h) and cold (c) plasma components, respectively, and k is the wave number [Baumjohann and Treumann, 2004, p. 264]. For comparison, on Figure 6 we have over-plotted the electron acoustic dispersion curve obtained from equation 2 with density and temperature parameters obtained from results from the "Cool" and "Drifting 2" populations of Table 3. However, we have increased the density of the Cool population to maintain a plasma frequency of 5.97 kHz. The two dispersion curves have a similar shape, but the plasma distribution used in the WHAMP analysis may also support weak beam modes, and perhaps more than one electron acoustic mode.

For this modeled phase space distribution, a sum of bi-Maxwellians (Figure 4b), Z-mode is not unstable. We proceed with a linear, cold plasma magnetoionic analysis using a kappa distribution, which can better describe a high energy tail.

Kappa Distribution Analysis

Kappa distributions have been shown to be a powerful tool for representing suprathermal components that deviate from Maxwellian distributions. [Vasyliunas, 1968; Feldman et al., 1975; Gosling et al., 1981; Yoon et al., 2013; Yoon, 2014]. The kappa model is numerically tractable and has numerous space plasma applications [cf. Livadiotis and McComas, 2013]. The phase space distribution shown in **Figure** 4a can also be modeled using an isotropic Maxwellian distribution, f_o, and a combination of an isotropic kappa distribution and an electron conic (or weak loss cone) distribution. Electric conics are distributions enhanced just outside the loss cone [Menietti et al., 1985]. The kappa distribution allows for increased energy of the extended tail of the distribution compared to a Maxwellian. We proceed as follows,

$$f = f_0 + f_h, \tag{3}$$

$$f_0 = \frac{n_0}{\pi^{3/2} w_0^3} \exp\left(-\frac{v^2}{w_0^2} \right), \tag{4}$$

$$f_h = \frac{n_h}{\pi^{3/2} (\kappa w^2)^{3/2} A} \frac{\Gamma(\kappa+1)}{\Gamma(\kappa - 1/2)} \frac{1}{(1 + v^2 / \kappa w^2)^{\kappa+1}} \left[1 - \tanh \frac{(\mu + \mu_0)^2}{\delta^2} + \Delta \left(1 + \tanh \frac{\mu + \mu_0}{\delta} \right) \right], \tag{5}$$

$$A = \frac{1}{2} \int_{-1}^{1} d\mu \left[1 - \tanh \frac{(\mu + \mu_0)^2}{\delta^2} + \Delta \left(1 + \tanh \frac{\mu + \mu_0}{\delta} \right) \right], \tag{6}$$

where f_o is the cool distribution, f_h is the warm distribution, v is electron kinetic speed, w_o is drift velocity, $\mu = \cos(\alpha)$ (α is the electron pitch angle), and $\Gamma(\kappa+1)$ is the gamma or factorial function. We choose the fitting parameters listed in Table 4.

The resulting phase space distribution is shown in Figure 7. A cut of the phase space distribution for the kappa distribution at a pitch angle of 109° is shown compared to the observations in Figure 7b. The Kappa model density is multiplied by the same factor of 6.2 as explained above for Figure 5. The Kappa distribution fits better at higher velocities compared to the bi-Maxwellian distribution. Analysis of this distribution proceeds according to linear magnetoionic wave dispersion theory as presented in Yoon [1996; 1998] and briefly summarized here. The wave dispersion relation for extraordinary (X), Z, and whistler (W) modes can be written,

$$N_{X/Z}^2 = 1 - \frac{f_{pe}^2}{f(f+\tau f_{ce})}, \quad N_{W/O}^2 = 1 - \frac{\tau f_{pe}^2}{f(\tau f - f_{ce}\cos^2\theta)}, \tag{7}$$

$$\tau = \left(s + \sqrt{s^2 + \cos^2\theta}\right)\frac{f_{pe}^2 - f^2}{\left|f_{pe}^2 - f^2\right|}, \quad s = \frac{f f_{ce}\sin^2\theta}{2\left|f_{pe}^2 - f^2\right|}, \tag{8}$$

where the various mode designations follow the customary practice based upon the range of wave frequency,

$$X \text{ mode: } f > f_X, \quad Z \text{ mode: } f_Z < f < f_Z^{\text{res}}, \tag{9}$$

$$O \text{ mode: } f > f_{pe}, \quad W \text{ mode: } 0 < f < f_W^{\text{res}}, \tag{10}$$

and where the various cutoffs and resonance frequencies are defined by

$$f_x = \frac{1}{2}\left(\sqrt{f_{ce}^2 + 4f_{pe}^2} + f_{ce}\right), \tag{11}$$

$$f_Z^{\text{res}} = \frac{1}{\sqrt{2}}\left[f_{pe}^2 + f_{ce}^2 + \sqrt{(f_{pe}^2 - f_{ce}^2)^2 + 4f_{pe}^2 f_{ce}^2\sin^2\theta}\right]^{1/2}, \tag{12}$$

$$f_W^{\text{res}} = \frac{1}{\sqrt{2}}\left[f_{pe}^2 + f_{ce}^2 - \sqrt{(f_{pe}^2 - f_{ce}^2)^2 + 4f_{pe}^2 f_{ce}^2\sin^2\theta}\right]^{1/2}, \tag{13}$$

and f_z was given previously in the Introduction.

The temporal growth rate is then expressed as

$$\gamma_\sigma = \frac{f_{pe}^2}{f}\frac{\pi^2}{R_\sigma}\sum_{s=0}^{\infty}\left(\Theta(sf_{ce} - f)\int_{-1}^{1} d\mu Q_s^\sigma(u_+,\mu) + \Theta(f - sf_{ce})\Theta(1-\mu_s^2)\int_{\mu_s}^{1} d\mu \sum_{+,-} Q_s^\sigma(u_\pm,\mu)\right), \tag{14}$$

where σ stands for *X*, *Z*, *W*, or *O*, and

$$Q_s^{X/Z}(u,\mu)=\frac{\tau^2}{\tau^2+\cos^2\theta}\frac{u^2(1-\mu^2)}{\left|u-N_{X/Z}\mu\cos\theta\right|}\left[\frac{f}{f_{ce}}\left(K_{X/Z}\sin\theta+\frac{\cos\theta}{\tau}(\cos\theta-N_{X/Z}u\mu)\right)\right.$$
$$\left.\times\frac{J_s(b)}{b}+J'_s(b)\right]^2\left(u\frac{\partial}{\partial u}+(N_{X/Z}u\cos\theta-\mu)\frac{\partial}{\partial\mu}\right)f(u,\mu), \tag{15}$$

$$Q_s^{W/O}(u,\mu)=\frac{1}{\tau^2+\cos^2\theta}\frac{u^2(1-\mu^2)}{\left|u-N_{W/O}\mu\cos\theta\right|}\left[\frac{f}{f_{ce}}\left(K_{W/O}\sin\theta\cos\theta-\tau(\cos\theta-N_{W/O}u\mu)\right)\right.$$
$$\left.\times\frac{J_s(b)}{b}+\cos\theta J'_s(b)\right]^2\left(u\frac{\partial}{\partial u}+(N_{W/O}u\cos\theta-\mu)\frac{\partial}{\partial\mu}\right)f(u,\mu), \tag{16}$$

$$u_\pm=N_\sigma\mu\cos\theta\pm\sqrt{N_\sigma^2\mu^2\cos^2\theta+2\left(\frac{sf_{ce}}{f}-1\right)}, \tag{17}$$

$$\mu_s=\frac{\sqrt{2}}{N_\sigma\cos\theta}\left(1-\frac{sf_{ce}}{f}\right)^{1/2},\quad b=\frac{f}{f_{ce}}N_\sigma u_\pm\sqrt{1-\mu^2}\sin\theta, \tag{18}$$

$$K_{X/Z}=\frac{f_{pe}^2}{f_{pe}^2-f^2}\frac{f_{ce}\sin\theta}{f+\tau f_{ce}},\quad K_{W/O}=\frac{f_{pe}^2}{f_{pe}^2-f^2}\frac{\tau f_{ce}\sin\theta}{\tau f-f_{ce}\cos^2\theta}. \tag{19}$$

For the kappa-loss-cone distribution the quantity of interest is

$$u\frac{\partial f}{\partial u}+(N_\sigma u\cos\theta-\mu)\frac{\partial f}{\partial\mu}=-\frac{n_h}{\pi^{3/2}(\kappa w^2)^{3/2}A}\frac{\Gamma(\kappa+1)}{\Gamma(\kappa-1/2)}$$
$$\times\left\{\frac{2u^2}{w^2}\frac{\kappa+1}{\kappa}\frac{1}{(1+v^2/\kappa w^2)^{\kappa+2}}\left[1-\tanh\frac{(\mu+\mu_0)^2}{\delta^2}+\Delta\left(1+\tanh\frac{\mu+\mu_0}{\delta}\right)\right]\right.$$
$$\left.+\frac{1}{(1+v^2/\kappa w^2)^{\kappa+1}}\frac{N_\sigma u\cos\theta-\mu}{\delta}\left(\frac{2(\mu+\mu_0)}{\delta}\mathrm{sech}^2\frac{(\mu+\mu_0)^2}{\delta^2}-\Delta\mathrm{sech}^2\frac{\mu+\mu_0}{\delta}\right)\right\}. \tag{20}$$

The growth rate superimposed on top of the dispersion surface is shown for both Z and W modes in Figure 8a. The individual surfaces are shown in Figures 8b,c, respectively. The free energy source of the Z-mode and whistler mode emission is the temperature anisotropy. Note that the W mode is unstable for $\omega/\Omega_e \sim 0.05$ (f ~ 1.5 kHz) for quasi-parallel propagation angles in a narrow range of frequencies. In contrast, the Z-mode is unstable for quasi-parallel directions over a broader range of frequencies closer to ω_{pe}. In Figure 9 we show the calculated growth rate as a function of frequency for three values of wave normal angle, θ, i.e. the angle between the wave vector, **k**, and the magnetic field. The Z-mode growth ranges from ~2 kHz to ~4.5 kHz for $\Gamma > 4.5 \times 10^{-4}$ kHz at wave normal angle near zero. The calculated Z-mode growth could explain the intense (red) emission of Figure 2b (03:15 to 04:30) and possible whistler mode emission (green) observed at lower frequencies in the same time interval.

The expected gain of the Z-mode emission can be estimated and is dependent on the radiation background levels. Some of the weakest observations of Z-mode emission during this event are seen earlier on the same day near 02:22 and within the frequency range 4 kHz < f < 5 kHz with spectral density ~2×10^{-13} $V^2m^2Hz^{-1}$. For typical values of Z-mode during the most intense emission, spectral densities are ~ 5×10^{-10} $V^2m^2Hz^{-1}$, therefore

$$G = I / I_o \sim 5x10^{-10} / 2\ x\ 10^{-13} = 2.5 \times 10^3 \quad (21)$$

$$G = exp\left(2\,\Gamma\tau_g\right) = 2.5 \times 10^3, \quad (22)$$

where Γ = temporal growth rate of the wave amplitude, and τ_g = growth time.

$$2\Gamma\tau_g = 7.8,\ \ \tau_g \sim 4s \quad (23)$$

We suspect that the phase space distribution we observe is relaxed from that which actually generated the waves, and thus the growth rate predicted from the measured distributions is smaller.

The whistler mode growth is quite weak and for a very narrow range of frequencies near 2 kHz. This is reasonably consistent with the observations, which show only weak whistler mode emission for $f < 3.5$ kHz.

We have investigated the growth rate of Z-mode at higher plasma densities, but at $\omega_{pe}/\Omega_{ce} > 0.35$ the Z-mode is damped except for cyclotron-maser emission near Ω_{ce}. We believe our choice of $\omega_{pe}/\Omega_{ce} = 0.21$ is reasonable, based on Langmuir Probe measurements and the temporal nature of the plasma population. The polarization of the Z-mode emission between 03:30 to 04:00, is left-handed indicating the Z-mode is propagating in a region where $\omega < \omega_{pe}$, consistent with our choice of f_{pe} ~6 kHz.

Summary and Conclusion

We have conducted a survey of possible source regions of 5 kHz narrow band Z-mode emission in the Saturn lower density region of the inner magnetosphere. Six such regions were chosen for further study, but only one region provided marginally sufficient sampling of electron pitch angles for determination of the phase space distribution. We have introduced two electron distributions. The first is a least-squares fit of the available PSD to a sum of bi-Maxwellians. This distribution contains no loss cone because none is directly observable possibly due to the limited coverage of the ELS anodes near the field-aligned direction and the 4-second sampling period. Analysis of this distribution with the WHAMP dispersion solver finds growth of electron acoustic waves but not of Z-mode waves. We then introduce a kappa distribution with a weak loss cone that is consistent with the data because of the observational uncertainties. For this distribution linear cold plasma magnetoionic theory [Yoon et al., 1996; 1998] is applied to discover wave growth for the Z-mode. We have identified a probable free energy source for the growth of Z-mode as a temperature anisotropy and a weak loss cone. The frequency range of the Z-mode is calculated to be approximately 2-5 kHz compared to the observed range of about 3-7 kHz, with the maximum frequency dependent on the plasma frequency of the source population. The modeled Z-mode growth rates are adequate to explain the observations with caveats. Whistler mode emission is also calculated to grow weakly in a narrow frequency range of a few hundred Hz near 2 kHz. Consistent with this, only weak whistler mode emission is observed for $f < 3.5$ kHz.

The region of the probable source, the inner edge of the Enceladus density torus and near magnetic field lines that map to the radiation belt can saturate some ELS anode measurements, and in the present case there are also anode obscuration difficulties. In addition, data are sampled over two distinct 4-second periods separated by approximately 3.5 minutes. These problems make the task of obtaining a sufficient electron phase space distribution very challenging. However, the time history of the event (cf. Figure 3) indicates a general pattern of consistently dominant electron phase space density in the anti-field-aligned direction. This provides confidence in the assumption of relatively constant PSD levels during the ~ 3.5 minutes separating the two sets of electron data (Sets A and B). The results suggest that narrow band emission, often observed in a frequency range centered near 5 kHz, can be generated by sources in the outer edge of the Enceladus torus, where the conditions $\omega_{pe}/\Omega_{ce} \lesssim .3$, $T_\perp/T_\parallel > 1$ and a weak loss cone are sufficient to support growth of the Z-mode. A source of temperature anisotropy near the Enceladus torus may be damping of ion cyclotron waves which have been identified and studied by many researchers [cf. Leisner et al., 2006; Menietti et al., 2013]. The narrow size of the source location may be due to the steep gradient in the density in this inner region of the Saturn magnetosphere. For the region of Z-mode growth analyzed in this work, the plasma $\beta \ll 1$. But as β increases nearer to the magnetic equator and the ring plane cyclotron and Landau damping of the Z-mode increase [cf. Gary, 1993]. Broadband electrostatic emission also increases in amplitude coincident with the onset of the intense Z-mode emission at ~ 03:15. The broadband emission is partially due to the electron acoustic mode (and possibly weak beam modes) generated by the observed plasma distribution, and probably also to the presence of dust impacts on the spacecraft antennas.

These studies provide a reasonable explanation for the presence of Z-mode emission in the inner magnetosphere of Saturn. Damping of and wave-particle interactions with this emission is a probable source of electron acceleration of electrons as suggested by Horne and Thorne [1998] for Earth, and Gu et al. [2013] and Menietti et al. [2015] for Saturn and should be the subject of further investigations.

Acknowledgments

We wish to thank J. Barnholdt for clerical assistance and J. Chrisinger for help with several figures. J.D.M. acknowledges support from NASA grant NNX11AM36G. In addition, J.D.M., D.P., and S-I.Y. acknowledge support from JPL contract 1415150. Cassini RPWS data are archived in calibrated, full resolution at the NASA Planetary Data System website: http//pds.nasa.gov/ds-view/pdsviewDataset.jsp?dsid=CO-V/E/J/s/SS-RPWS-3-RDR-LRFULL-

V1.0. Observations of the CAPS/ELS instrument and the magnetic field instrument MAG on Cassini are available at http://ppi.pds.nasa.gov. P.H.Y. acknowledges NSF grant AGS1550566 to the University of Maryland and the support by the BK21 plus program through the National Research Foundation (NRF) funded by the Ministry of Education of Korea, to Kyung Hee University, Korea. He also acknowledges the Science Award Grant from the GFT Foundation to the University of Maryland. O.S. acknowledges support from the LH14010 grant and from the Praemium Academiae award.

References

Albert, J. M. (2007), Refractive index and wavenumber properties for cyclotron resonant quasilinear diffusion by cold plasma waves, *Phys. Plasmas, 14*, 072901, doi:10.1063/1.2744363.

Arridge, C. S., L. K. Gilbert, G. R. Lewis, E. C. Sittler, G. H. Jones, D. O. Kataria, A. J. Coates, D. T. Young (2009), The effect of spacecraft radiation sources on electron moments from the Cassini CAPS electron spectrometer, *Plan. Space Sci, 57*, 854-868, doi:10.1016/j.pss.2009.02.011.

Benson, R. F., P. A. Webb, J. L. Green, D. L. Carpenter, V. S. Sonwalkar, H. G. James, and B. W. Reinisch (2006), Active wave experiments in space plasmas: The Z Mode, in *Geospace Electromagnetic Waves and Radiation*, edited by J. W. LaBelle and R. A. Treumann, pp. 3-35, Springer, Berlin, doi:10.1007/3-540-33203-0_1.

Bevington, Philip R. (1969), *Data Reduction and Error Analysis for the Physical Sciences, pp. 235-242,* McGraw-Hill Book Company, New York.

Coates, A. J., C. Alsop, A. J. Coker, D. R. Linder, A. J. Johnstone, R. D. Woodliffe, M. Grande, A. Preece, S. Burge, D. S. Hall (1996), The electron spectrometer for the Cassini spacecraft, *J. British Interplanetary Soc., 45* (9).

Connerney, J. E. P., N. F. Ness, and M H. Acuna (1982), Zonal harmonic model of Saturn's magnetic field from Voyager 1 and 2 observations, *Nature, 298*, 44-46, doi:10.1038/298044a0.

Dougherty, M. K., et al. (2004), The Cassini magnetic field investigation, Space Sci. Rev., 114, 331-383, doi:10.1007/s11214-004-1432-2.

Gary, S. Peter (1993), *Theory of Space Plasma Microinstabilities*, Cambridge Atmospheric and Space Science Series, Cambridge University Press, New York, pp. 112-116.

Glauert, S. A., and R. B. Horne (2005), Calculation of pitch angle and energy diffusion coefficients with the PADIE code, *J. Geophys. Res., 110*, A04206, doi:10.1029/2004JA010851.

Gu, X., R. M. Thorne, B. Ni, and S.-Y. Ye (2013), Resonant diffusion of energetic electrons by narrowband Z mode waves in Saturn's inner magnetosphere, *Geophys. Res. Lett., 40,* 255-261, doi:10.1029/2012GL054330.

Gurnett, D. A., S. D. Shawhan, and R. R. Shaw (1983), Auroral hiss, Z-mode radiation, and auroral kilometric radiation in the polar magnetosphere: DE 1 observations, *J. Geophys. Res., 88*, No. A1, 329-340.

Gurnett, D. A., and A. Bhattacharjee (2005), Introduction to Plasma Physics, Cambridge

University Press, Cambridge, p. 124, doi:10.1017/CBO9780511809125.

Gurnett, D. A., W. S. Kurth, D. L. Kirchner, G. B. Hospodarsky, T. F. Averkamp, P. Zarka, A. Lecacheux, R. Manning, A. Roux, P. Canu, N. Cornilleau-Wehrlin, P. Galopeau, A. Meyer, R. Boström, G. Gustafsson, J.-E. Wahlund, L. Åhlén,H. O. Rucker, H. P. Ladreiter, W. Macher, L. J. C. Woolliscroft, H. Alleyne, M. L. Kaiser, M. D. Desch, W. M. Farrell, C. C. Harvey, P. Louarn, P. J. Kellogg, K. Goetz, and A. Pedersen (2004), The Cassini radio and plasma wave investigation, *Space Sci. Rev., 114,* 395-463, doi:10.1007/s11214-004-1434-0.

Horne, R. B., and R. M. Thorne (1998), Potential waves for relativistic electron scattering and stochastic acceleration during magnetic storms, *Geophys. Res. Lett., 25*(15), 3011-3014, doi:10.1029/98GL01002.

Kurth, W. S. (1982), Detailed observations of the source of terrestrial narrowband electromagnetic radiation. *Geophys. Res. Lett., 9,* 1341-1344, doi:10.1029/GL009i012p01341.

Kurth, W. S., T. F. Averkamp, D. A. Gurnett, and Z. Wang (2006), Cassini RPWS observations of dust in Saturn's E Ring, *Plan. Space Science, 54*, 988-998, doi:10.1016/j.pss.2006.05.011.

Leisner, J. S., C. T. Russell, M. K. Dougherty, X. Blanco-Cano, R. J. Strangeway, and C. Bertucci (2006), Ion cyclotron waves in Saturn's E ring: Initial Cassin observations, *Geophys. Res. Lett., 33*, L11101, doi:10.1029/2005GL024875.

Livadiotis, G., and D. J. McComas (2013), Understanding kapa distributions: A toolbox for space science and astrophysics, *Space Sci. Rev., 175*, 183-214, doi:10.1007/s11214-013-9982-9.

Menietti, J. D., and J. L. Burch (1985), Electron Conic" signatures observed in the nightside auroral zone and over the polar cap, *J. Geophys. Res., 90*(A6), 5345–5353, doi:10.1029/JA090iA06p05345.

Menietti, J. D., P. Schippers, Y. Katoh, J. S. Leiser, G. B. Hospodarsky, D. A. Gurnett, and O. Santolik (2013), Saturn chorus intensity variations, *J. Geophys. Res. Space Physics, 118*, 5592-5602, doi:10.1002/jgra.50529.

Menietti, J. D., T. F. Averkamp, J. B. Groene, R. B. Horne, Y. Y. Shprits, E. E. Woodfield, G. B. Hospodarsky, and D. A. Gurnett (2014), Survey analysis of chorus intensity at Saturn, *J. Geophys. Res. Space Physics, 119,* 8415-8425, doi:10.1002/2014JA020523.

Menietti, J. D., T. F. Averkamp, S.-Y. Ye, R. B. Horne, E. E. Woodfield, Y. Y. Shprits, D. A. Gurnett, A. M. Persoon, and J.-E. Wahlund (2015), Survey of Saturn Z-mode emission, *J. Geophys. Res. Space Physics, 120,* 6176-6187, doi:10.1002/2015JA021426.

Persoon, A. M., D. A. Gurnett, J. S. Leisner, W S. Kurth, J. B. Groene, and J. B. Faden (2013), The plasma density distribution in the inner region of Saturn's magnetosphere, *J. Geophys.*

Res. Space Physics, 118, 2970-2974, doi:10.1002/jgra.50182.

Rönnmark, K. (1982), WHAMP waves in a homogeneous anisotropic multi-component plasma, Rep. 179, Kiruna Geophys. Inst., Kiruna, Sweden.

Rönnmark, K. (1983), Computation of the dielectric tensor of a Maxwellian plasma, *Plasma Phys., 25*(6), 699-701, doi:10.1088/0032-1028/25/6/007.

Shprits, Y. Y., J. D. Menietti, X. Gu, K. C. Kim, and R. B. Horne (2012), Gyroresonant interactions between the radiation belt electrons and whistler mode chorus waves in the radiation environments of Earth, Jupiter, and Saturn: A comparative study, *J. Geophys. Res., 117*, A11216, doi:10.1029/2012JA018031.

Vasyliunas, V. M. (1968), A survey of low-energy electrons in the evening sector of the magnetosphere with OGO 1 and OGO 3, *J. Geophys. Res., 73*(9), 2839-2884, doi:10.1029/JA073i009p02839.

Wahlund, J.-E., et al. (2005), The inner magnetosphere of Saturn: Cassini RPWS cold plasma results from the first encounter, *Geophys Res. Lett., 32*, L20509, doi:10.1029/2005GL022699.

Wahlund, J.-E., M. André, A. I. E. Eriksson, M. Lundberg, M. W. Morooka, M. Shafiq, T. F. Averkamp, D. A. Gurnett, G. B. Hospodarsky, W. S. Kurth, K. S. Jacobsen, A. Pedersen, W.

Farrell, S. Ratynskaia, N. Piskunov (2009), Detection of dusty plasma near the E-ring of Saturn, *Plan. Space Science, 57*, 1795-1806, doi:10.1016/j.pss.2009.03.011.

Xiao, F., S. Zhang, Z. Su, Z. He, and L. Tang (2012), Rapid acceleration of radiation belt energetic electrons by Z-mode waves, *Geophys. Res. Lett., 39*, L03103, doi:10.1029/2011GL050625.

Ye, S.-Y., J. D. Menietti, G. Fischer, Z. Wang, B. Cecconi, D. A. Gurnett, and W. S. Kurth (2010), Z mode waves as the source of Saturn narrowband radio emissions, *J. Geophys. Res., 115*, A08228, doi:10.1029/2009JA015167.

Ye, S.-Y., D. A. Gurnett, W. S. Kurth, T. F. Averkamp, M. Morooka, S. Sakai, and J.-E. Wahlund (2014), Electron density inside Enceladus plume inferred from plasma oscillations excited by dust impacts, *J. Geophys. Res. Space Physics, 119,* 3373-3380, doi:10.1002/2014JA019861.

Yoon, P. H. (2014), Electron kappa distribution and quasi-thermal noise, *J. Geophys. Res. Space Physics, 119,* 7074-7087, doi:10.1002/2014JA020353.

Yoon, P. H., A. T. Weatherwax, T. J. Rosenberg, and J. LaBelle (1996), Lower ionospheric cyclotron maser theory: A possible source of $2f_{ce}$ and $3f_{ce}$ auroral radio emissions, *J. Geophys. Res., 101*(A12), 27015-27025, doi:10.1029/96JA02664.

Yoon, P. H., A. T. Weatherwax, and T. J. Rosenberg (1998), On the generation of auroral radio emissions at harmonics of the lower ionospheric electron cyclotron frequency: X, O and Z mode maser calculations, *J. Geophys. Res., 103*(A3), 4071-4078, doi:10.1029/97JA03526.

Yoon, P. H., L. F. Ziebell, R. Gaelzer, L. Wang, and R. P. Lin (2013), Solar wind electron acceleration via Langmuir turbulence, *Terr. Atmos. Ocean. Sci., 24*, 175-182, doi:10.3319/TAO.2012.05.30.01(SEC).

Young, D. T., et al. (2004), Cassini plasma spectrometer investigation, *Space Sci. Rev., 114*, 1-112, doi:10.1007/s11214-004-1406-4.

Table 1

Probable Z-mode (5-kHz) Source Regions

Year	DOY	Northern start	Northern stop	Southern start	Southern stop
2008	168	03:20	04:30		
2008	182	07:30	08:10	09:15	10:10
2008	196	09:00	09:55	10:45	11:50
2008	203	10:15	10:50	11:40	12:30
2009	223			11:00	12:10
2010	027	05:00	06:30		

Table 2

Selected ELS Anodes

Centerline Pitch Angle (degs) of Anodes

	Hr:Mn:Sec	deg	deg	deg	deg	deg
Set A	03:31:59	168*	167*	149	129	109
Set B	03:35:43	87	67	47	27	8

* Indicates Partially Obstructed

Table 3

Bi-Maxwellian Fit to Observations

Population	n(m^{-3})**	$w_\parallel$(m/s)	$T_\perp/T_\parallel$	V_{drft}(m/s)
Cool	2.97 x 10^5 (.63)*	8.75 x 10^5 (.29)	0.861 (.56)	0.0
Warm 1	4.57 x 10^4 (.89)	3.12 x 10^6 (.37)	0.603 (.81)	0.0
Warm 2	1.38 x 10^4 (.71)	1.45 x 10^7 (.59)	0.629 (.94)	0.0
Drifting 1	6.27 x 10^4 (.63)	1.02 x 10^6 (.48)	4.40 (.74)	1.5 x 10^6
Drifting 2	2.50 x 10^4 (.63)	4.76 x 10^6 (.39)	1.82 (.70)	3.0 x 10^6

** (Calculated Value)/6.2 * percent uncertainty in parentheses

Table 4

Kappa Fit Parameters

w_o(m/s)	n_h(m^{-3})	μ_0	δ	Δ	κ
1.02x10^6	4.42x10^5	0.1	0.6	0.3	1

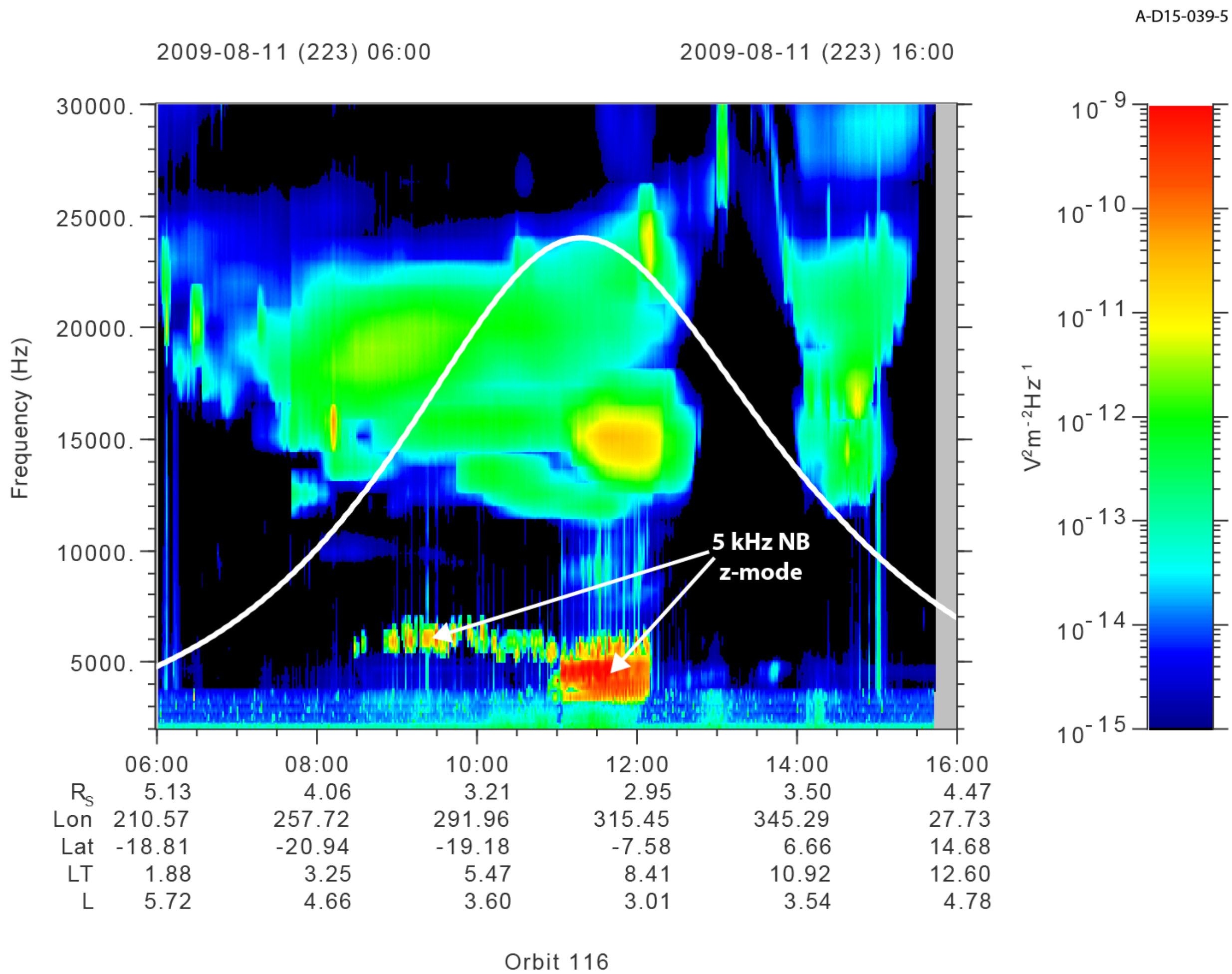

Figure 1

A spectrogram of Z-mode emission for day 223 of 2008, indicative of a probable source region. This emission is intense, narrow-banded centered near 5 kHz, $\omega < \Omega_{ce}$. Note the intense Z-mode (~ 11:00 to ~ 12:15) is also coincident with intense, broad-banded electrostatic emission (green color). The white line is the electron cyclotron frequency.

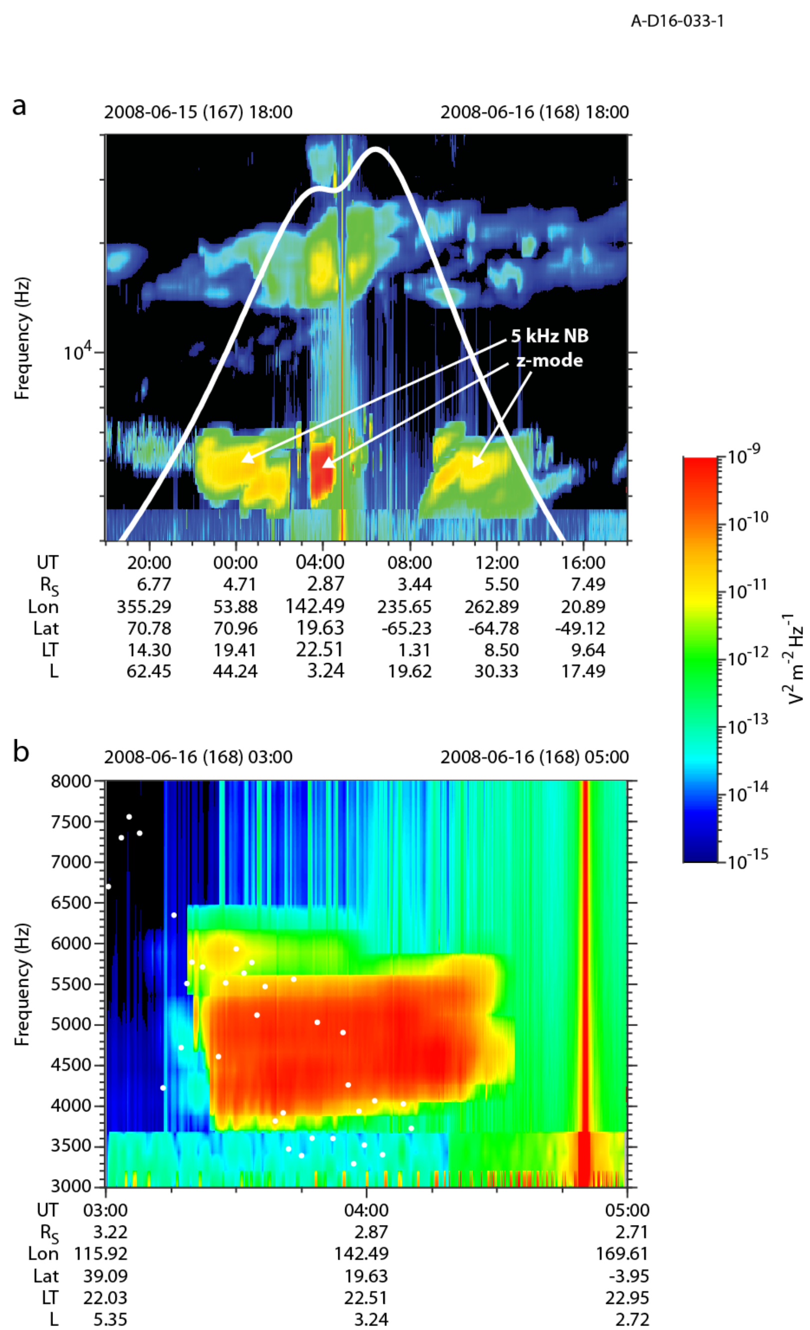

Figure 2

a) Narrow band (NB) Z-mode emission observed on day 167-168, 2008, centered near 5 kHz with the most intense emission observed at lower latitudes as the density increases and broadband electrostatic emission becomes intense (~03:00-04:30). The white line is the cyclotron frequency. b) a higher resolution plot of the most intense emission centered near 5 kHz. The intense, narrow in time, broadband emission near 04:50 is the signature of the ring plane crossing near the magnetic equator. The white dots are ~ 1 minute averages of the plasma frequency obtained from the Langmuir Probe.

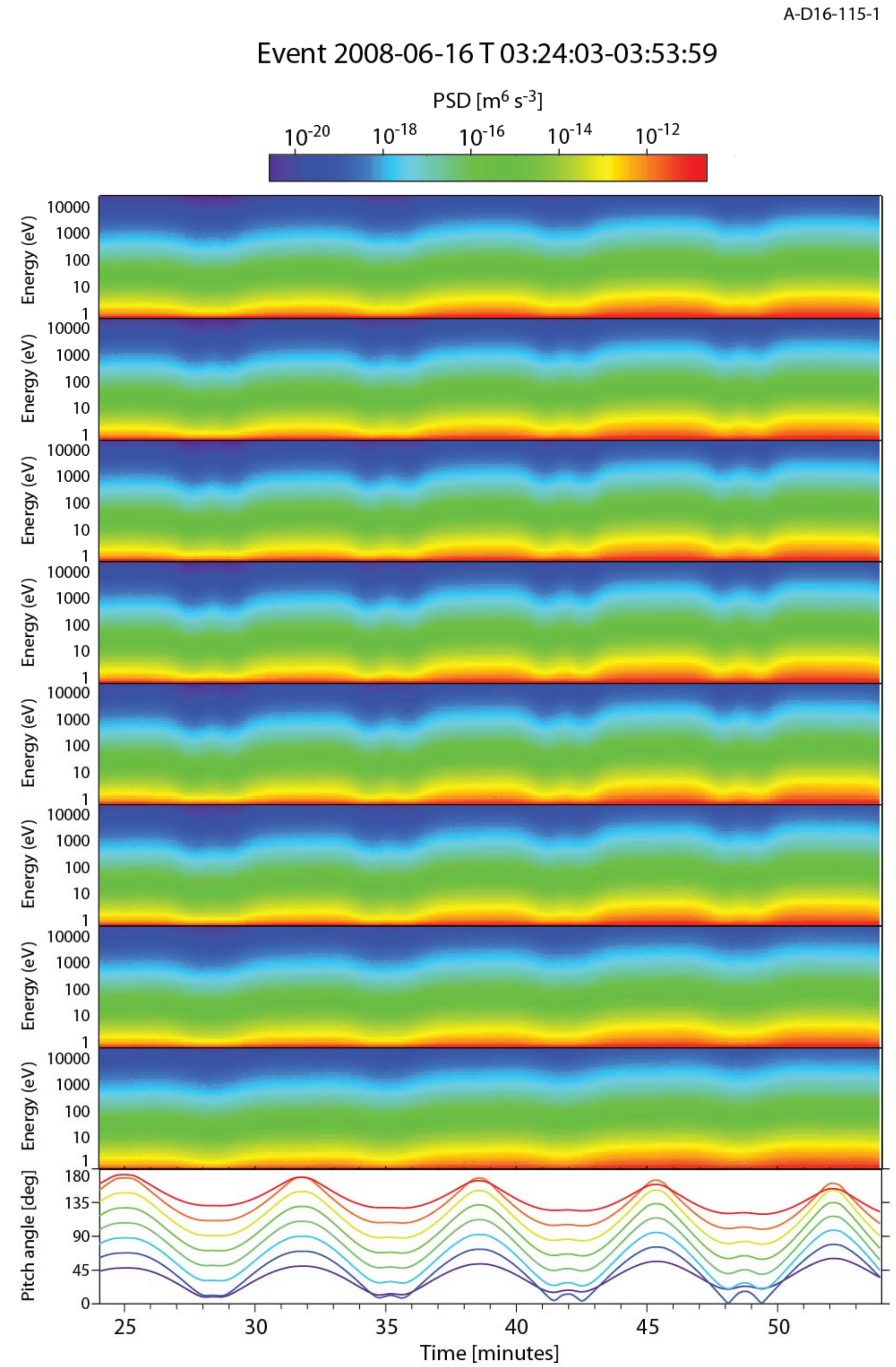

Figure 3

Electron phase space density (PSD) as a function of time during the intense emission shown in Figure 3. All eight anode of ELS are plotted, with the pitch angle (α) of each anode in the bottom panel. The pattern is similar for each anode, showing a decrease in electron PSD for pitch angles near 0°, and a slow increase in overall peak energy as a function of time. The time axis units are minutes after the start time (3 hr 24 min 3 sec).

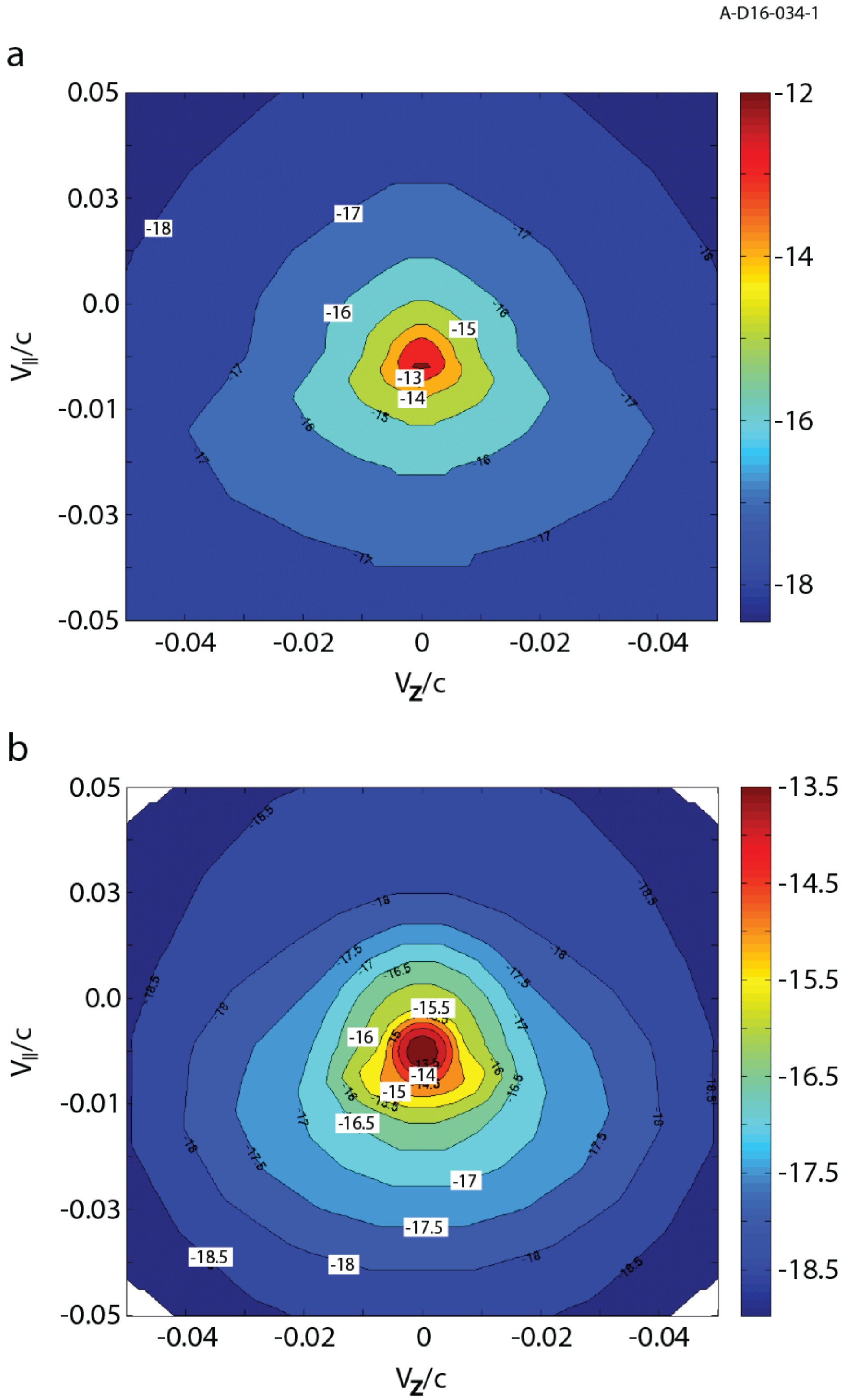
A-D16-034-1
a
0.05
0.03
0.0
-0.01
-0.03
-0.05
-0.04
-0.02
0
-0.02
-0.04
V||/c
VZ/c
-12
-14
-16
-18
-18
-17
-16
-15
-13
-14
b
0.05
0.03
0.0
-0.01
-0.03
-0.05
-0.04
-0.02
0
-0.02
-0.04
V||/c
VZ/c
-13.5
-14.5
-15.5
-16.5
-17.5
-18.5
-15.5
-16
-14
-15
-16.5
-17
-17.5
-18.5
-18

Figure 4

a) Phase space density (PSD) after mirroring the data about the $V_{\parallel}$ axis. The color bar units are log{PSD (sec^3/m^6)}. For the anti-field-aligned direction note a distinct increase in electron particle flux and a temperature anisotropy. b) Least-squares fit model distribution using the data from Table 3.

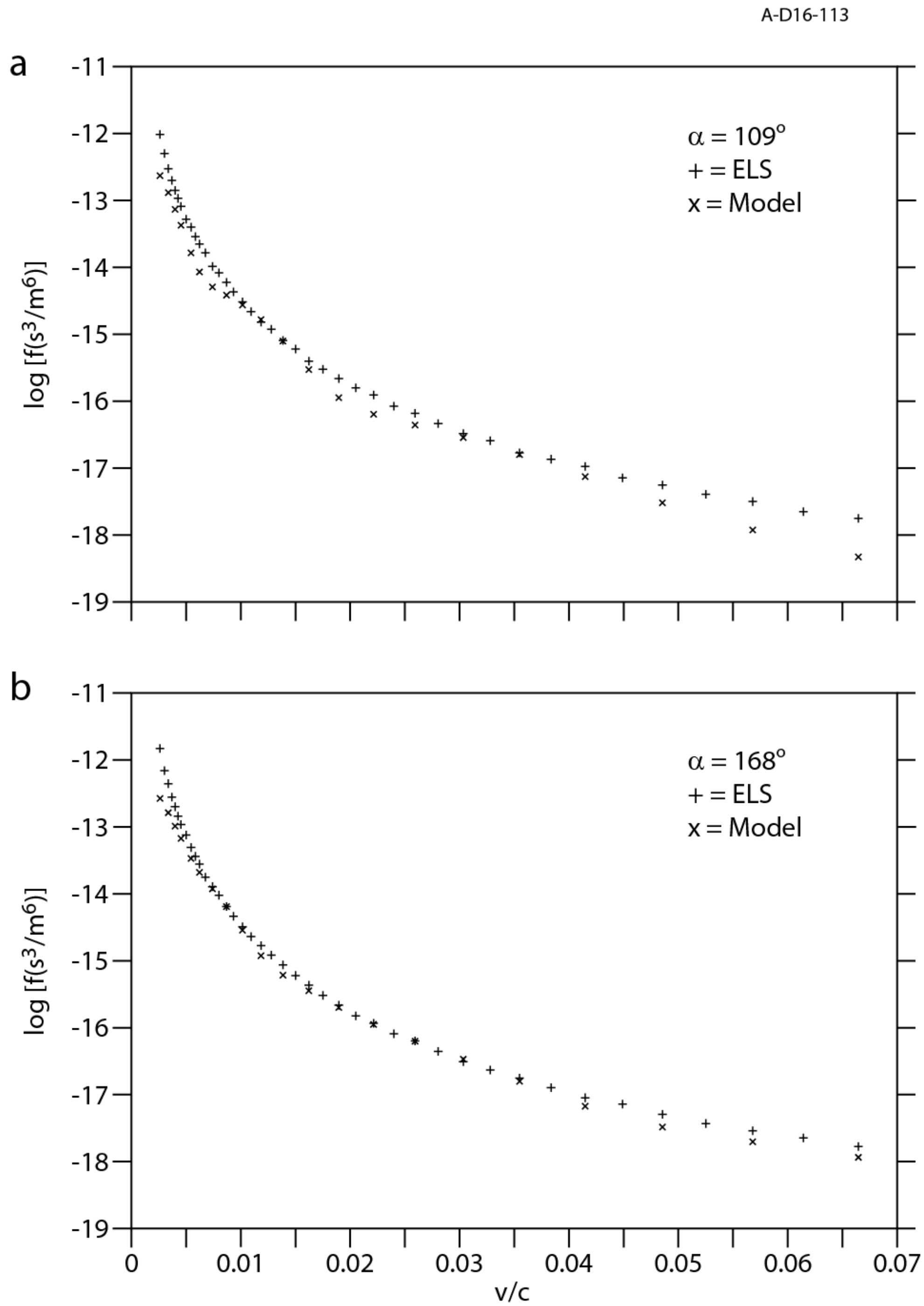

556

557 **Figure 5**

558 Cuts of the observed and model PSD at pitch angles (α) of a) 109° and b) 168° as labelled.

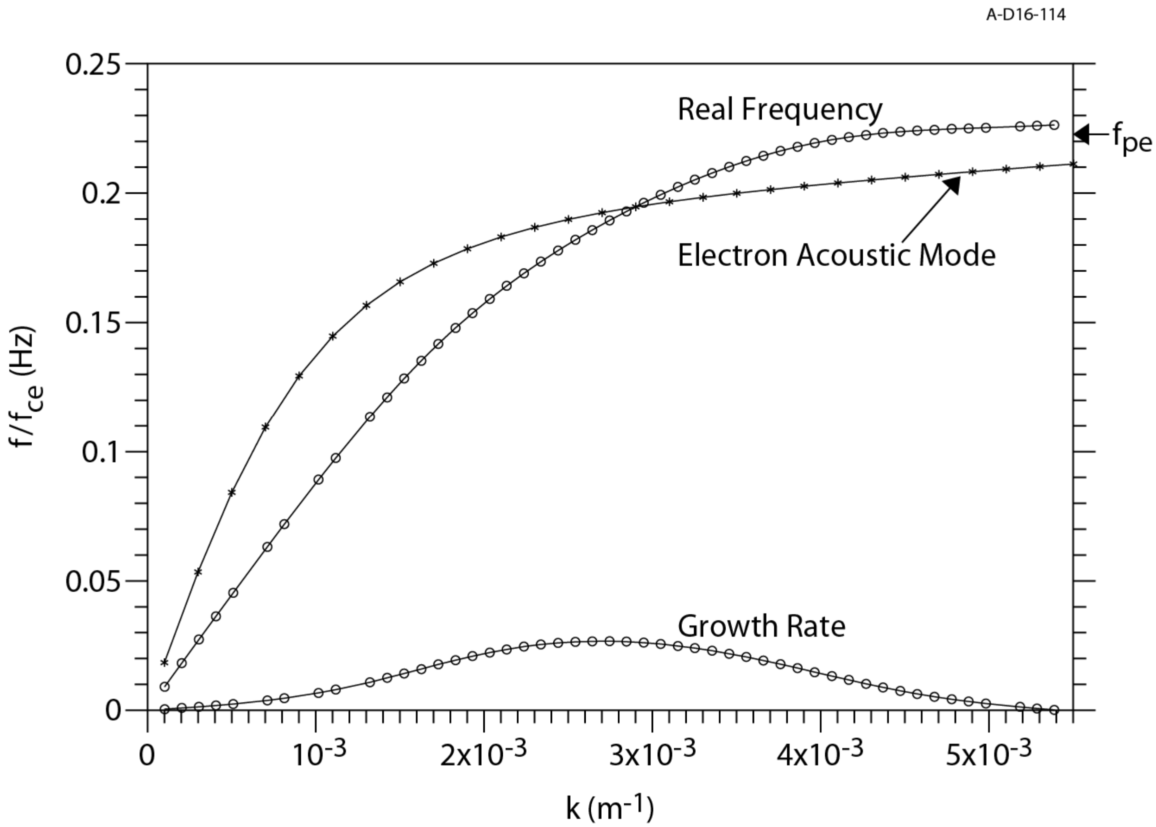

Figure 6

Dispersion and growth curves for the WHAMP analysis showing a broad spectrum with maximum growth near 5 kHz and damping near f_{pe}. These waves are reasonably narrow-banded with a peak near 5 kHz. Also plotted is the dispersion curve for the elctron acoustic mode resulting from equation 2.

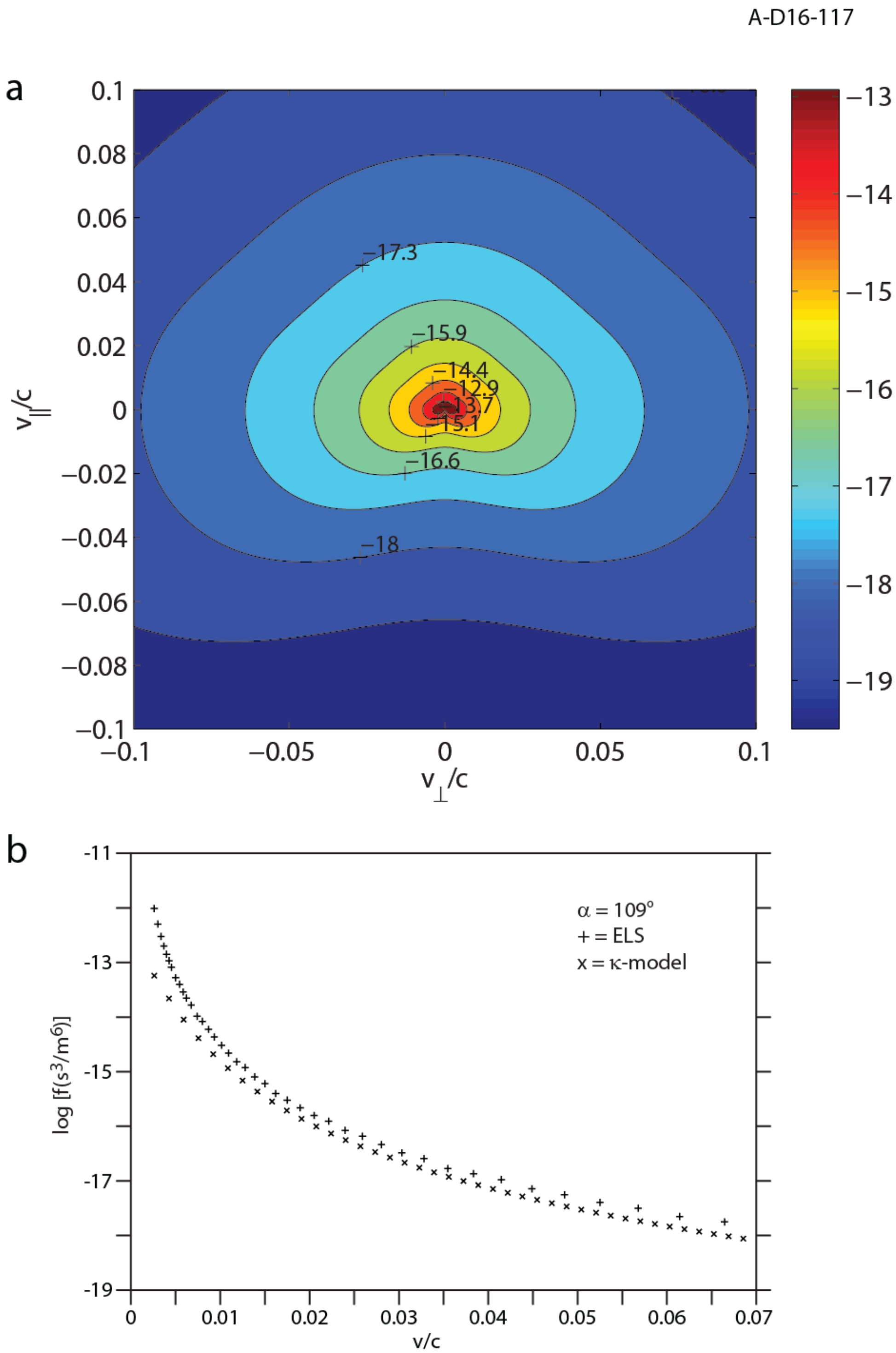

Figure 7

(a) Phase space distribution using a combination of an isotropic kappa distribution and an electron conic (or weak loss cone) distribution. Parameters are listed in Table 4. (b) Cuts of the observed and model PSD at pitch angle $\alpha = 109°$ for the kappa distribution as labelled. Note the better fit at larger velocities compared to the bi-Maxwellian fit of Figure 5 for the same pitch angle.

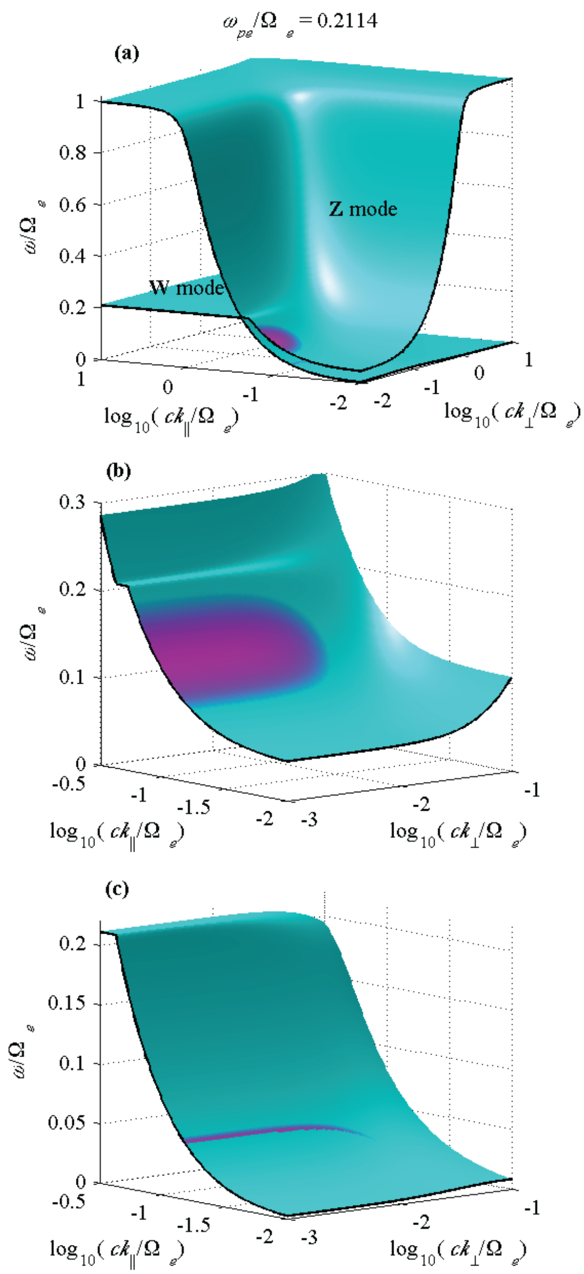

Figure 8

We choose ω_{pe}/Ω_e = 0.2144 corresponding to f_{pe} = 6 kHz and obtain the dispersion surfaces shown in Figure 8a. Growth rate superimposed on top of the dispersion surface is shown for both Z and W modes in 7b,c, respectively.

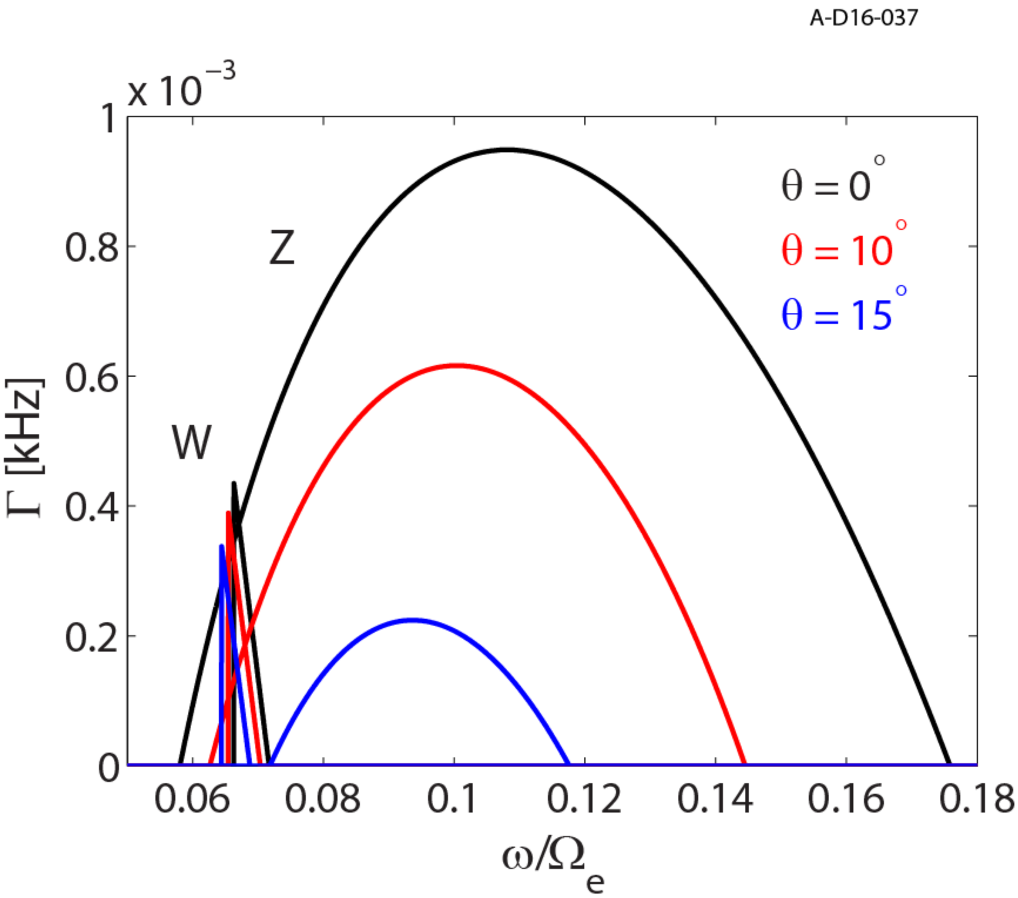

Figure 9

Temporal growth rate as a function of frequency for three wave normal angles.

Figure 1.

A-D15-039-5

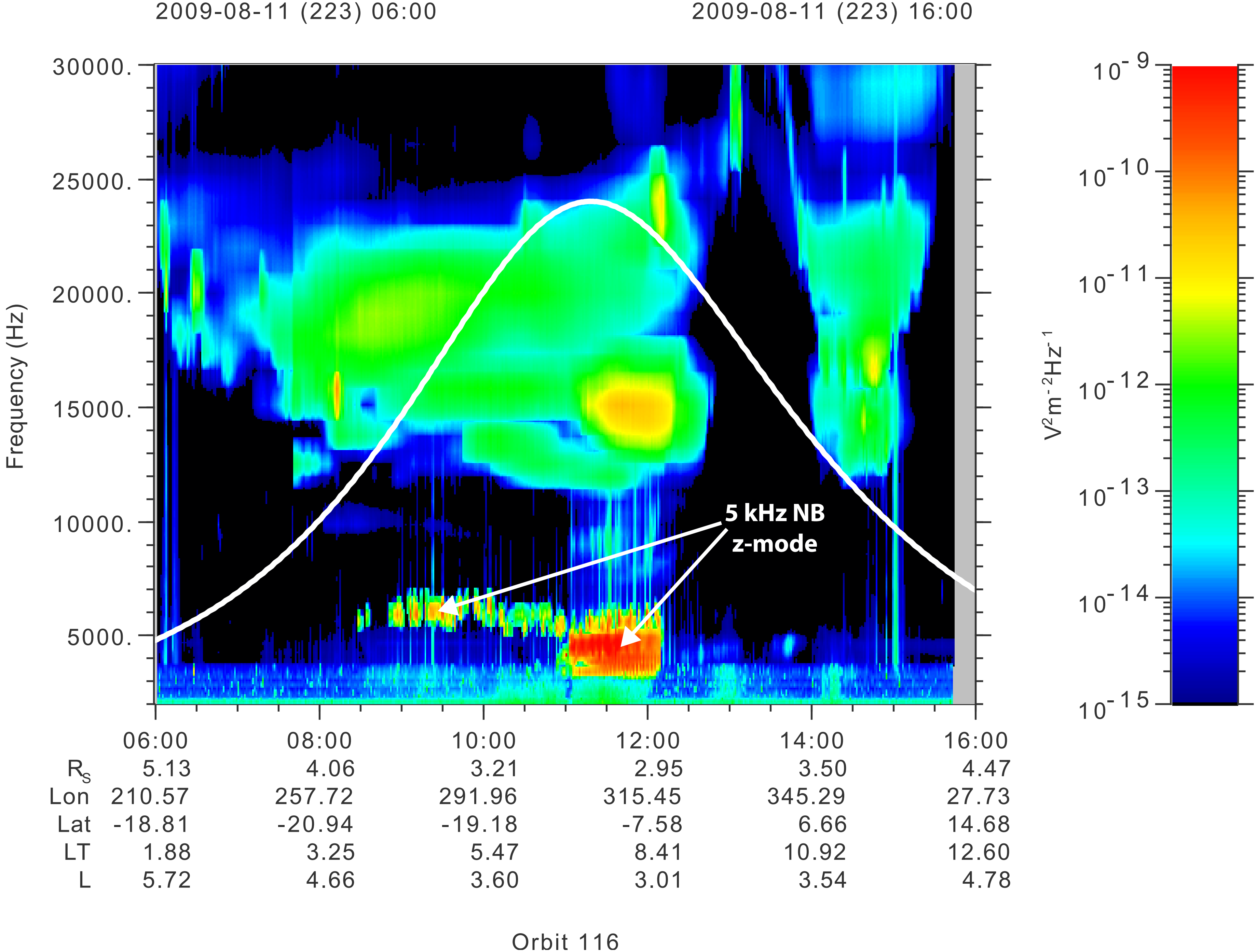

2009-08-11 (223) 06:00
2009-08-11 (223) 16:00
Frequency (Hz)
30000.
25000.
20000.
15000.
10000.
5000.
5 kHz NB
z-mode
$V^2m^{-2}Hz^{-1}$
10^{-9}
10^{-10}
10^{-11}
10^{-12}
10^{-13}
10^{-14}
10^{-15}
06:00
08:00
10:00
12:00
14:00
16:00
R_S 5.13 4.06 3.21 2.95 3.50 4.47
Lon 210.57 257.72 291.96 315.45 345.29 27.73
Lat -18.81 -20.94 -19.18 -7.58 6.66 14.68
LT 1.88 3.25 5.47 8.41 10.92 12.60
L 5.72 4.66 3.60 3.01 3.54 4.78
Orbit 116

Figure 2.

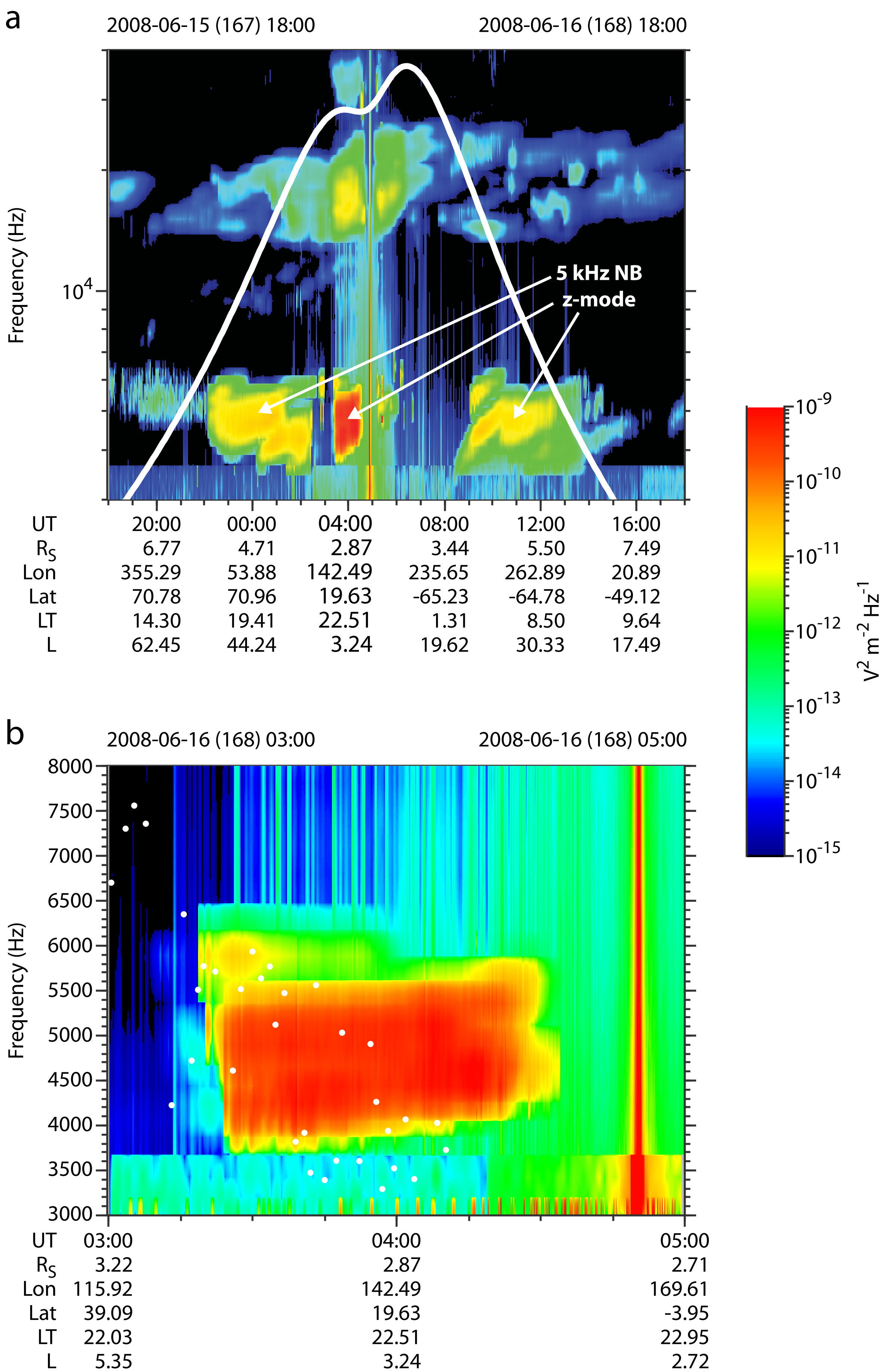
a
2008-06-15 (167) 18:00
2008-06-16 (168) 18:00
Frequency (Hz)
10^4
5 kHz NB
z-mode
UT 20:00 00:00 04:00 08:00 12:00 16:00
RS 6.77 4.71 2.87 3.44 5.50 7.49
Lon 355.29 53.88 142.49 235.65 262.89 20.89
Lat 70.78 70.96 19.63 -65.23 -64.78 -49.12
LT 14.30 19.41 22.51 1.31 8.50 9.64
L 62.45 44.24 3.24 19.62 30.33 17.49
b
2008-06-16 (168) 03:00
2008-06-16 (168) 05:00
Frequency (Hz)
8000 7500 7000 6500 6000 5500 5000 4500 4000 3500 3000
UT 03:00 04:00 05:00
RS 3.22 2.87 2.71
Lon 115.92 142.49 169.61
Lat 39.09 19.63 -3.95
LT 22.03 22.51 22.95
L 5.35 3.24 2.72
10^-9 10^-10 10^-11 10^-12 10^-13 10^-14 10^-15
V^2 m^-2 Hz^-1

Figure 3.

A-D16-115-1

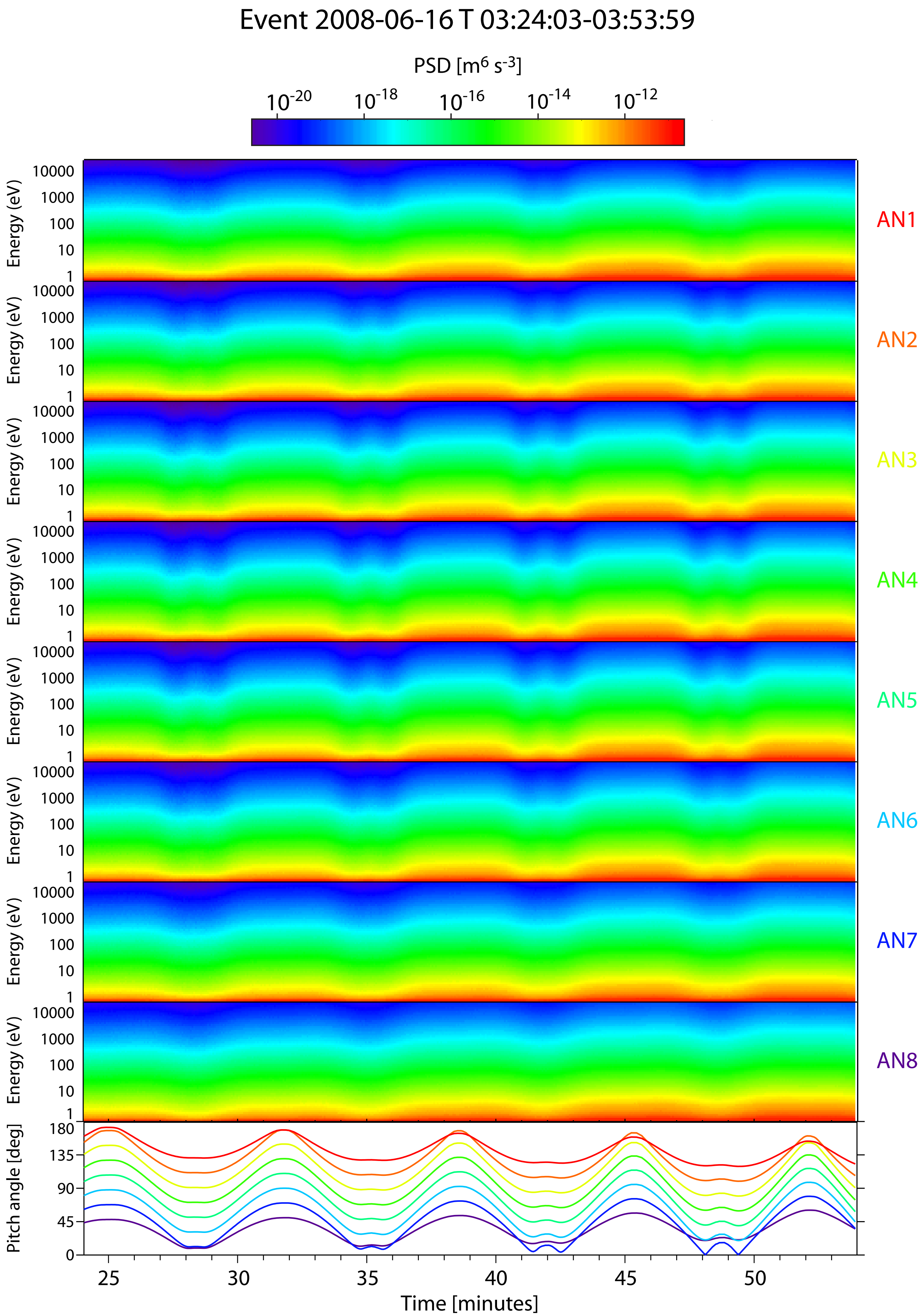

Event 2008-06-16 T 03:24:03-03:53:59
PSD [m6 s-3]
10-20
10-18
10-16
10-14
10-12
Energy (eV)
10000
1000
100
10
1
AN1
AN2
AN3
AN4
AN5
AN6
AN7
AN8
Pitch angle [deg]
180
135
90
45
0
25
30
35
40
45
50
Time [minutes]

Figure 4.

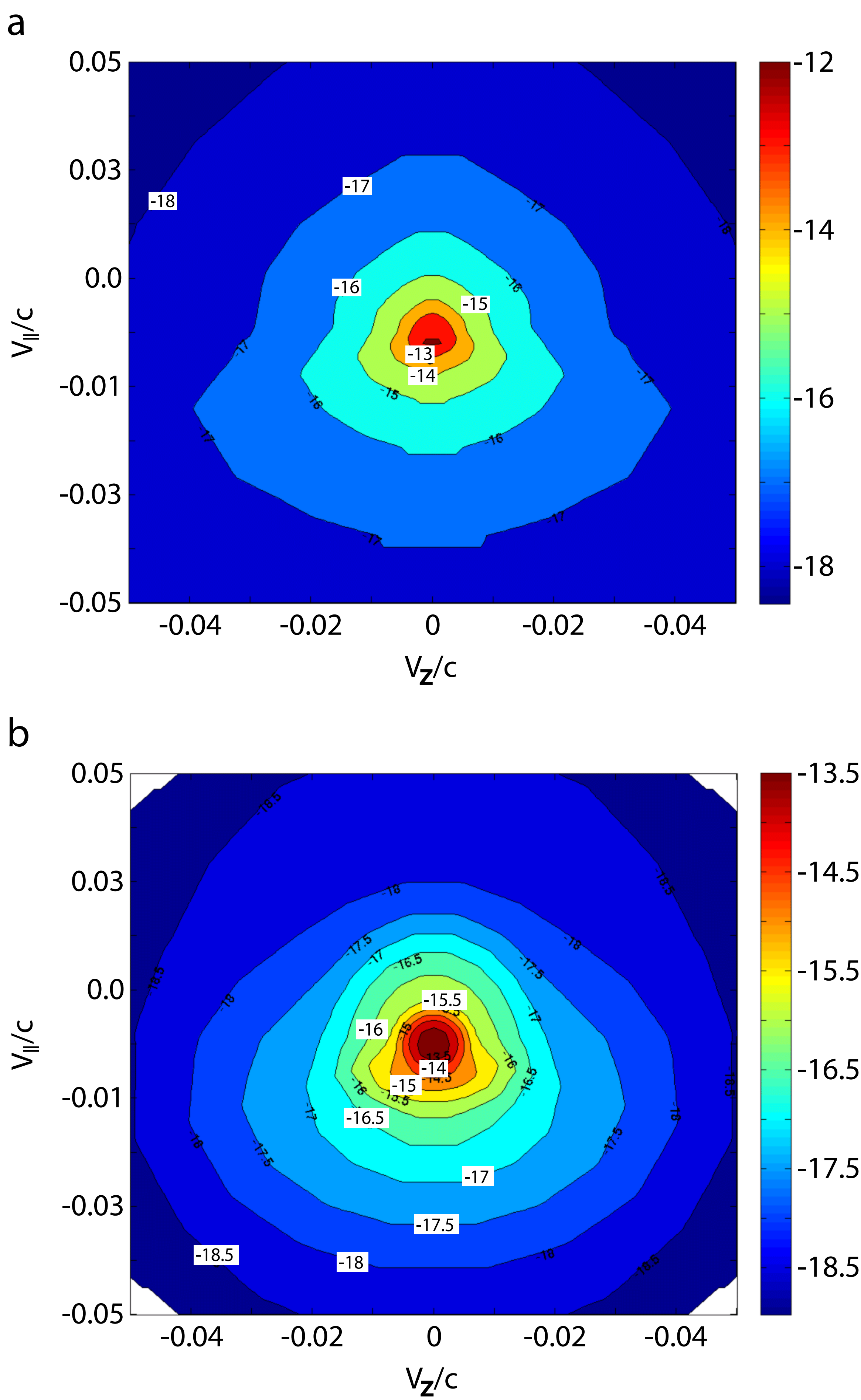
a
0.05
0.03
0.0
-0.01
-0.03
-0.05
V||/c
-0.04
-0.02
0
-0.02
-0.04
Vz/c
-12
-14
-16
-18
-18
-17
-16
-15
-13
-14
b
0.05
0.03
0.0
-0.01
-0.03
-0.05
V||/c
-0.04
-0.02
0
-0.02
-0.04
Vz/c
-13.5
-14.5
-15.5
-16.5
-17.5
-18.5
-15.5
-16
-14
-15
-16.5
-17
-17.5
-18.5
-18

Figure 5.

A-D16-113

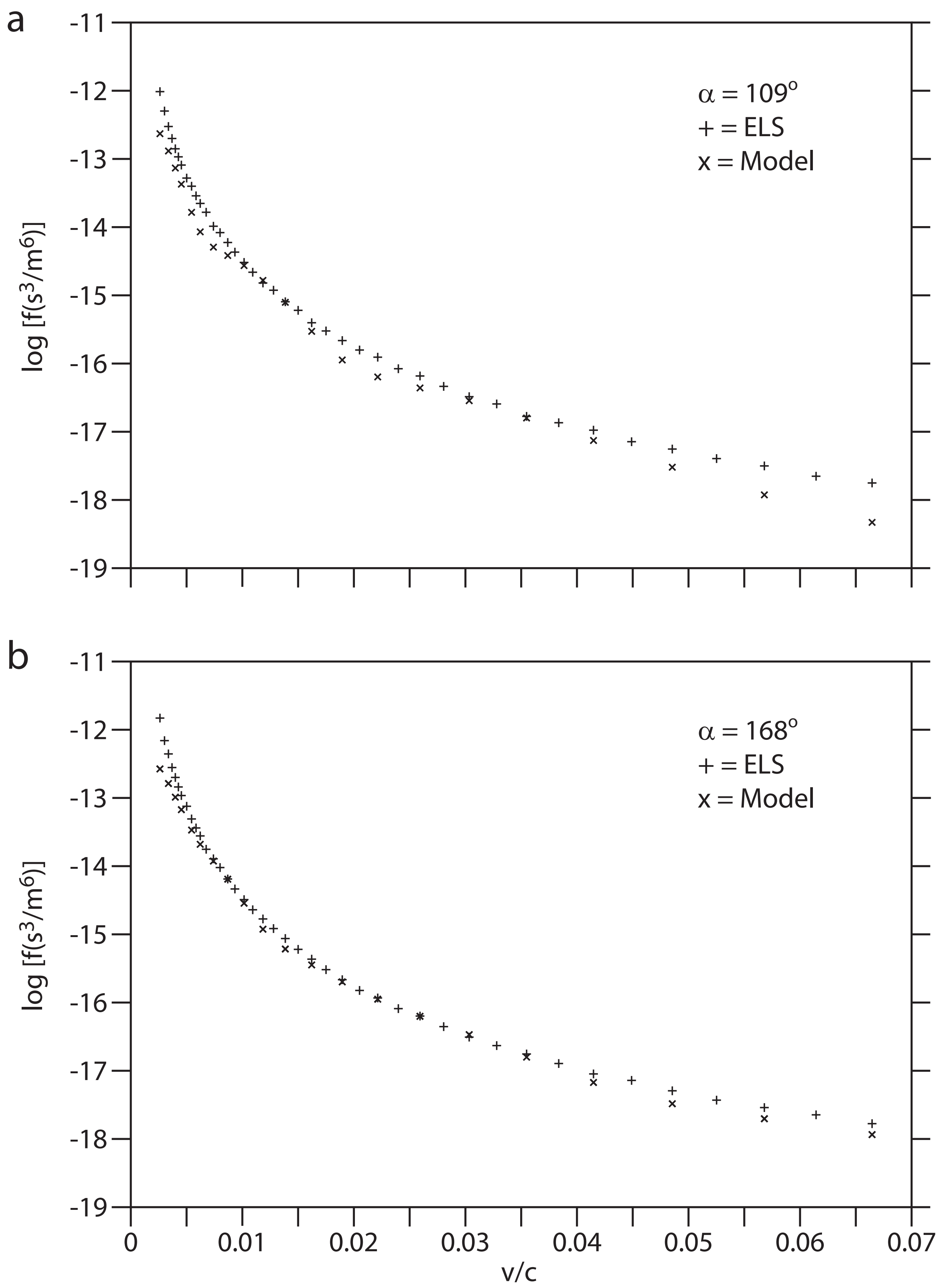

a
log [f(s^3/m^6)]
-11
-12
-13
-14
-15
-16
-17
-18
-19
α = 109°
+ = ELS
x = Model
b
α = 168°
+ = ELS
x = Model
0
0.01
0.02
0.03
0.04
0.05
0.06
0.07
v/c

Figure 6.

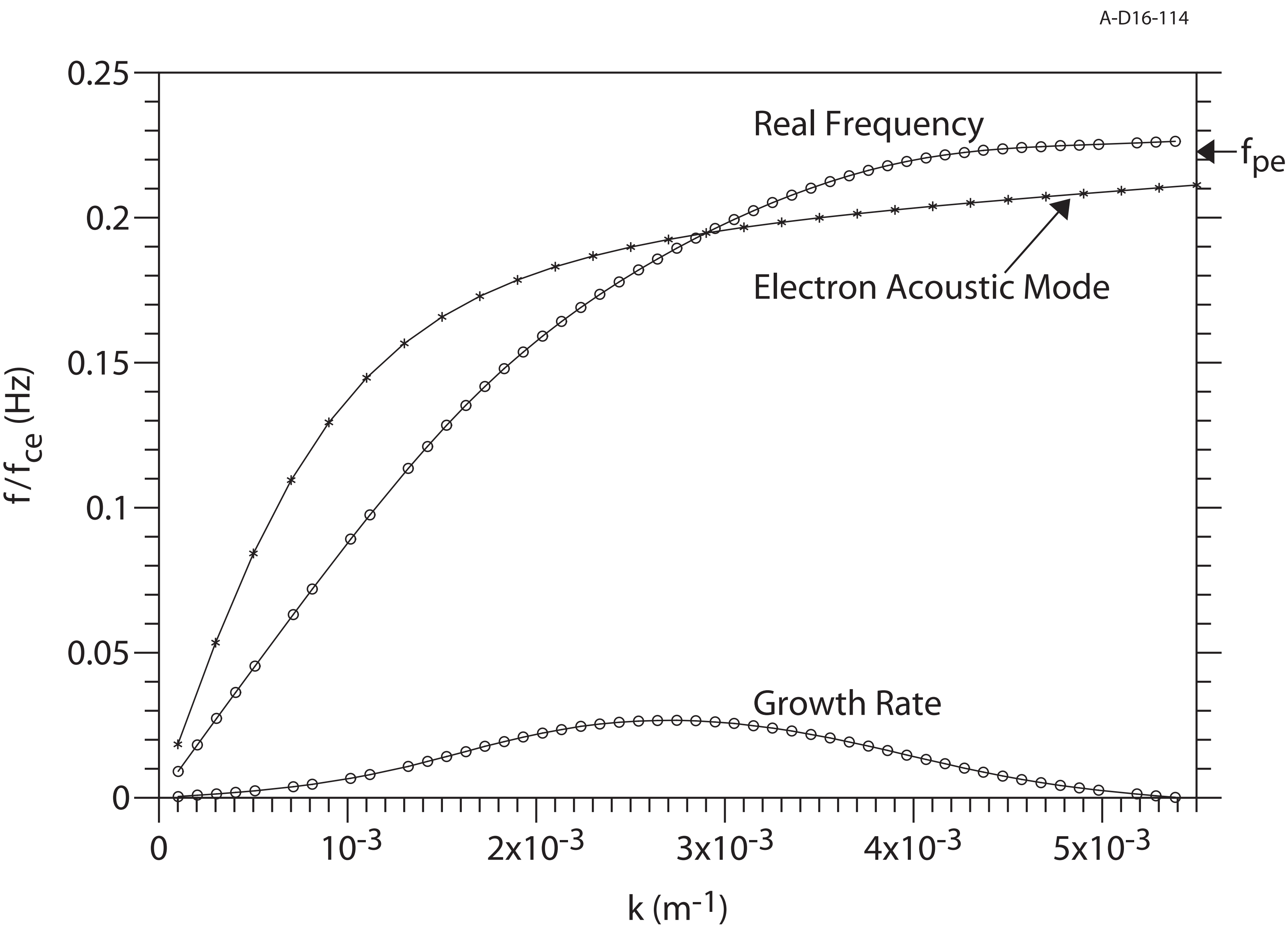
A-D16-114
Real Frequency
Electron Acoustic Mode
Growth Rate
f_pe
f/f_ce (Hz)
k (m^-1)
0.25
0.2
0.15
0.1
0.05
0
0
10^-3
2x10^-3
3x10^-3
4x10^-3
5x10^-3

Figure 7.

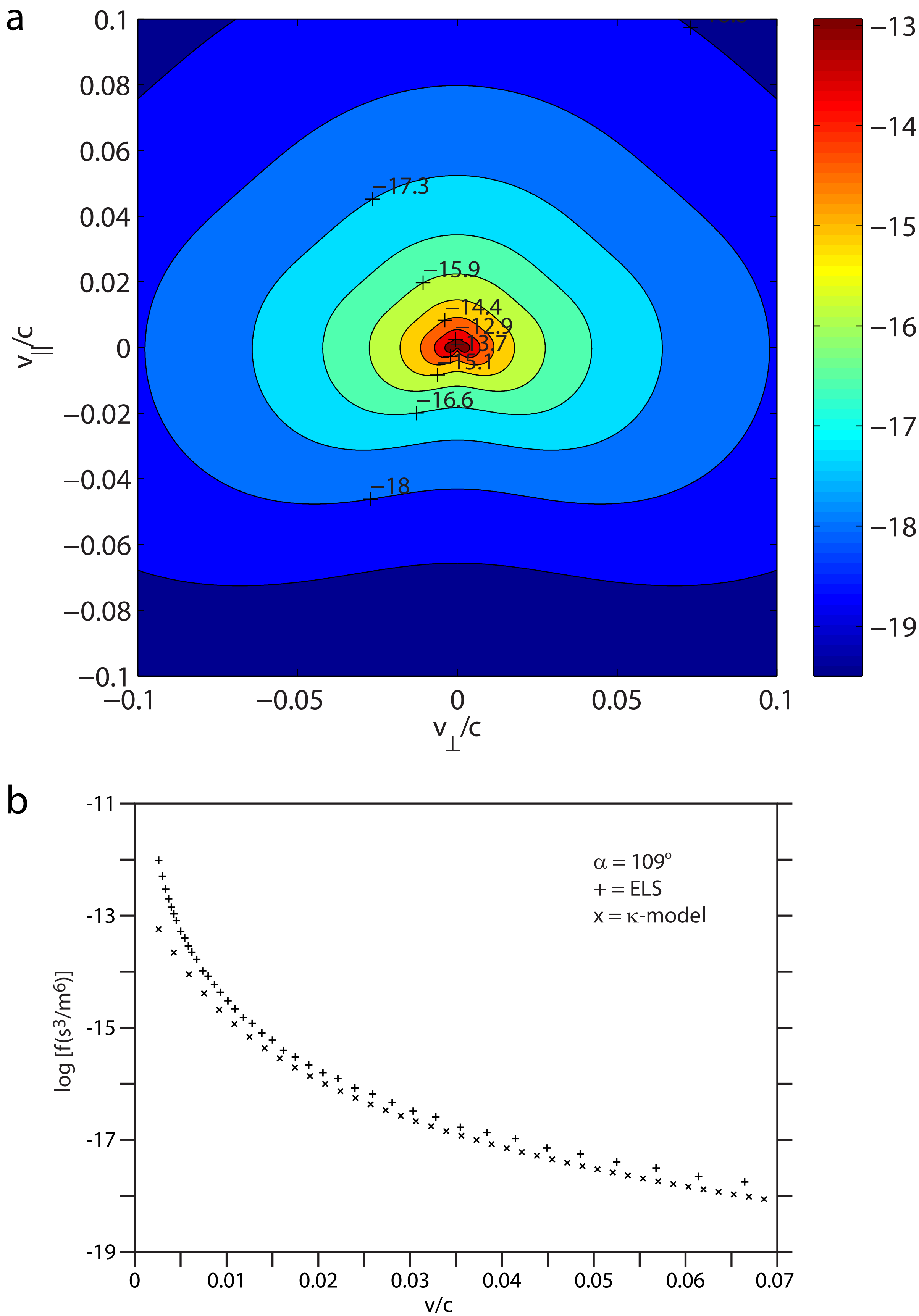
a
0.1
0.08
0.06
0.04
0.02
0
−0.02
−0.04
−0.06
−0.08
−0.1
$v_{||}/c$
−0.1
−0.05
0
0.05
0.1
$v_{\perp}/c$
−17.3
−15.9
−14.4
−12.9
−13.7
−15.1
−16.6
−18
−13
−14
−15
−16
−17
−18
−19
b
-11
-13
-15
-17
-19
log [f(s³/m⁶)]
0
0.01
0.02
0.03
0.04
0.05
0.06
0.07
v/c
α = 109°
+ = ELS
x = κ-model

Figure 8.

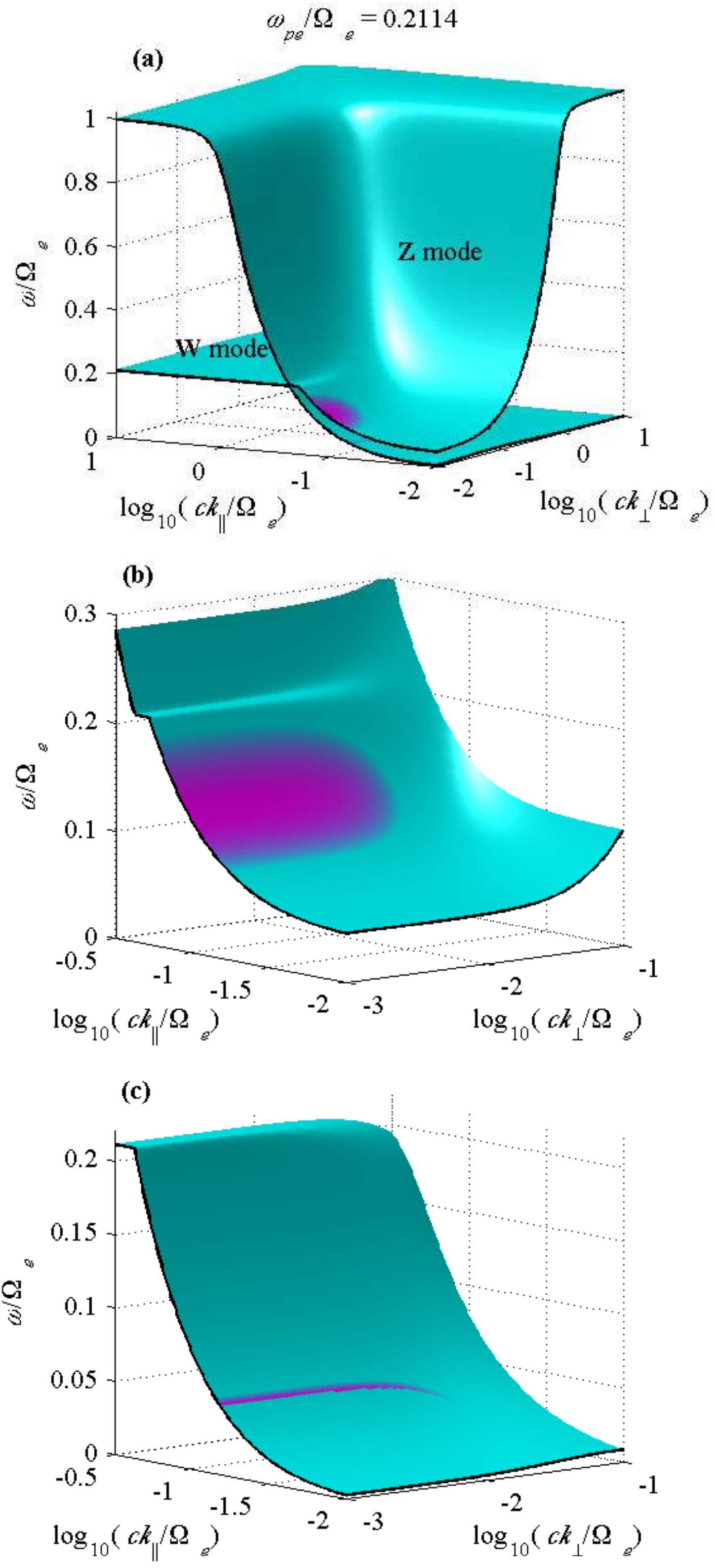

ωpe/Ωe = 0.2114
(a)
Z mode
W mode
ω/Ωe
1
0.8
0.6
0.4
0.2
0
1
0
-1
-2
log10(ck∥/Ωe)
-2
-1
0
1
log10(ck⊥/Ωe)
(b)
ω/Ωe
0.3
0.2
0.1
0
-0.5
-1
-1.5
-2
log10(ck∥/Ωe)
-3
-2
-1
log10(ck⊥/Ωe)
(c)
ω/Ωe
0.2
0.15
0.1
0.05
0
-0.5
-1
-1.5
-2
log10(ck∥/Ωe)
-3
-2
-1
log10(ck⊥/Ωe)

Figure 9.

A-D16-037

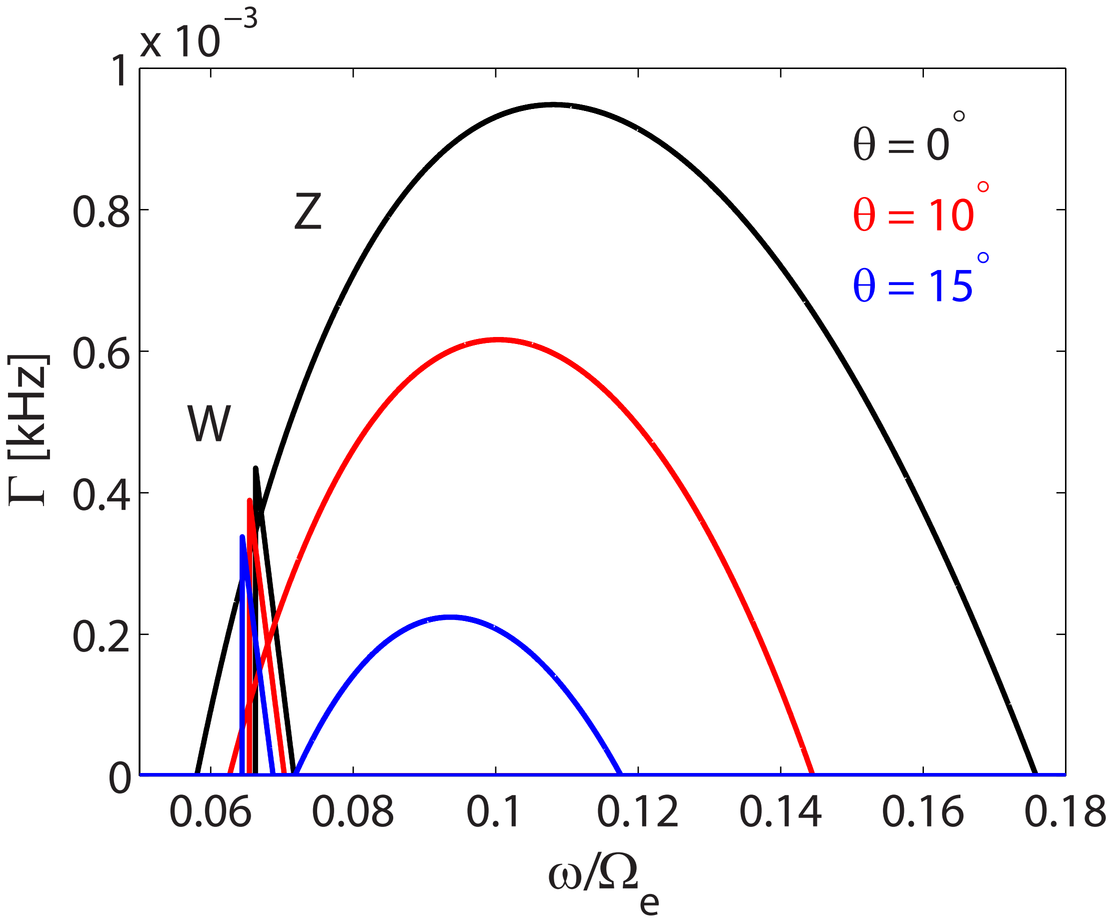

x 10^-3
1
0.8
0.6
0.4
0.2
0
Γ [kHz]
0.06
0.08
0.1
0.12
0.14
0.16
0.18
ω/Ω_e
W
Z
θ = 0°
θ = 10°
θ = 15°

Table 1

Probable Z-mode (5-kHz) Source Regions

Year	DOY	Northern		Southern	
		start	stop	start	stop
2008	168	03:20	04:30		
2008	182	07:30	08:10	09:15	10:10
2008	196	09:00	09:55	10:45	11:50
2008	203	10:15	10:50	11:40	12:30
2009	223			11:00	12:10
2010	027	05:00	06:30		

Table 2

Selected ELS Anodes

Centerline Pitch Angle (degs) of Anodes

	Hr:Mn:Sec	deg	deg	deg	deg	deg
Set A	03:31:59	168*	167*	149	129	109
Set B	03:35:43	87	67	47	27	8

* Indicates Partially Obstructed

Table 3

Bi-Maxwellian Fit to Observations

Population	n(m^{-3})**	$w_{\parallel}$(m/s)	$T_{\perp}/T_{\parallel}$	V_{drft}(m/s)
Cool	2.97×10^5 (.63)*	8.75×10^5 (.29)	0.861 (.56)	0.0
Warm 1	4.57×10^4 (.89)	3.12×10^6 (.37)	0.603 (.81)	0.0
Warm 2	1.38×10^4 (.71)	1.45×10^7 (.59)	0.629 (.94)	0.0
Drifting 1	6.27×10^4 (.63)	1.02×10^6 (.48)	4.40 (.74)	1.5×10^6
Drifting 2	2.50×10^4 (.63)	4.76×10^6 (.39)	1.82 (.70)	3.0×10^6

** (Calculated Value)/6.2   * percent uncertainty in parentheses

Table 4

Kappa Fit Parameters

w_o(m/s)	n_h(m^{-3})	μ_0	δ	Δ	κ
1.02×10^6	4.42×10^5	0.1	0.6	0.3	1